Spatiotemporal variability of turbulent fluxes in snow-covered mountain terrain

Rainette Engbers

6128742

MSc. Climate Physics

Institute for Marine and Atmospheric Research Utrecht
UNIVERSITEIT UTRECHT

Supervisors
Prof. Michiel VAN DEN BROEKE, Utrecht University
Dr. Sergi GONZALEZ-HERRERO, SLF
Prof. Michael LEHNING, SLF

Contents

Abstract

Turbulent exchange of heat and moisture plays an important role in snow cover dynamics in mountain regions and governs boundary layer dynamics. Although these processes are subject to great spatial and temporal variability, especially in complex terrain, measurements of heat, moisture, and momentum fluxes are almost exclusively point observations. To quantify the spatial variability, and assess the representativeness of the observations, numerical modeling of the atmosphere and surface is a useful tool. Nevertheless, there is considerable uncertainty regarding the accuracy of surface models in capturing turbulent fluxes, particularly in complex terrain with large spatial variability on small scales. These uncertainties can be attributed in part to (1) the use of Monin-Obukhov similarity theory, which has limitations in complex terrain because the assumptions of stationarity and spatial homogeneity are usually not fulfilled and (2) the errors in representing wind speeds and near-surface atmospheric gradients in the simulations. In this study, we analyze sources of errors in representing energy exchange over snow in mountain areas by models and specifically look at the spatio-temporal variability during different meteorological events in the region of Davos, Switzerland. To verify common modeling approaches with observations, we use model predictions of turbulent fluxes from CRYOWRF, the atmospheric model WRF coupled to the surface model SNOWPACK. The fluxes at different resolutions are compared to turbulent fluxes measured using the eddy covariance method and calculated with the Monin-Obukhov similarity theory. This model comparison and spatial analysis is carried out for three different meteorological events that are representative of the local climate, particularly föhn events. The results from the model indicate that the fluxes vary strongly spatially. Depending on the weather pattern, elevation plays a large role in the variability of the turbulent fluxes, and they correlate by elevation with wind speed. This shows that local turbulent heat fluxes are not representative of the whole mountain area. This has implications for the calculation of snow melt, sublimation, and accumulation across mountainous terrain. The model resolution also plays an important role in the representation of fluxes, as coarser (1 km) resolutions greatly overestimate wind speeds compared to higher resolutions (200 m). This is due to fewer topography-wind interactions resulting in an overestimation of turbulent fluxes.

1 Introduction

Interactions between the atmosphere and the surface play a crucial role in shaping the temporal evolution of snow cover over mountainous regions. The main drivers of snow ablation are controlled by spatially variable shortwave radiation, longwave radiation, and turbulent exchange of heat and moisture (Mott et al., 2011). Therefore, an accurate representation of turbulent fluxes is essential for modeling the mass and energy balance of snowpacks, which, in turn, is critical for predicting the snow hydrological cycle, avalanche hazards, and climate in cold regions.

One key to deriving the turbulent fluxes correctly is to adequately represent the wind field in heterogeneous topography (Mott et al., 2018). Knowledge of wind fields in mountain terrain, like valley and slope winds, speed-up over ridges, and thermodynamic structures is well established. However, when it comes to modeling or characterizing turbulence over highly complex terrain, the same assumptions are made as over flat and horizontally homogeneous terrain (Rotach & Zardi, 2007). Even in state-of-the-art numerical weather models, these parametrizations are implemented. At low resolutions, the smoothing of topography to reduce numerical instabilities makes these assumptions more valid. However, with increasing resolution, the need for better parametrization of turbulent surface fluxes in complex terrain is important.

Furthermore, snow-covered surfaces strongly influence the character of the boundary layer, leading to the development of highly stable boundary layers due to radiative cooling or advection of warm air over a colder surface (Schlögl et al., 2017). Stable stratified boundary layers weaken turbulence and decoupling between surface layers can occur. In general, they are less well understood than their unstable counterparts (Mahrt, 2014).

Despite the variability of turbulent fluxes over terrain (Lehner & Rotach, 2018), nearly all measurements of turbulent exchange of heat and moisture in snow - atmosphere interactions are point measurements. On a small spatial scale, Haugeneder et al. (2023) used a high-resolution thermal infrared camera to investigate the spatial variability of the near-surface atmospheric layer dynamics. On a large spatial scale, an analysis of numerical models can be used to gain a deeper understanding of the processes influencing these interactions. Particularly, research during synoptic flow-induced weather patterns in mountain regions, such as föhn, remains limited. Some case studies compared numerical simulations with data during föhn events, which showed that the models are not yet capable of correctly representing turbulent processes (Gohm et al., 2004) and the subsequent erosion of a cold-air-pool in valleys (Umek et al., 2021).

There are several models capable of simulating wind-induced snow distribution processes (Gauer, 1999; Lehning et al., 2008; Naaim et al., 1998). These models have two components: a surface model, which simulates the snowpack and estimates the threshold wind speed for snow transport, and an atmospheric model, which simulates the 3D wind field at high spatial resolution. However, in these models the two components are not coupled, subsequently, the wind field drives the snowpack model which redistributes the snow. Recently, fully coupled snowpack and atmospheric models have been developed, for example, Meso-NH/Crocus (Vionnet et al., 2014) and CRYOWRF (Sharma et al., 2021). These works highlight the importance of snow redistribution and blowing snow sublimation for the total mass balance of the snowpack. However, there remains a gap in the literature regarding the spatial variability of turbulent sensible and latent heat fluxes within such high-resolution coupled models.

Therefore, the following work aims to enhance our understanding of the variability of turbulent fluxes on snow-covered mountain terrain during different weather patterns typical for the Alps, specifically during south and north föhn events. To perform this analysis, we used the novel state-of-the-art model CRYOWRF, a coupled atmosphere-snowpack model. First, we compare the model to point measurements of turbulent fluxes in complex terrain to assess if the fluxes are correctly represented in the model. Secondly, we look at the variability of these fluxes over the terrain, focusing especially on the differences induced by the different synoptic weather patterns. Third, we investigate the effect of the model resolution on the prediction of turbulent fluxes, for resolutions of 1 km and 200 m. Finally, we address the limitations of the model, including the choice of roughness length and applicability of the Monin-Obukhov similarity theory in complex terrain.

2 Theory

2.1 Basic equations for turbulent motions

The basis for calculating turbulent heat fluxes stems from the Navier-Stokes equations representing the conservation of mass, momentum, heat, and moisture:

$$\begin{aligned}
\frac{\partial u_j}{\partial x_j} &= 0 \\
\frac{\partial u_i}{\partial t} + u_j\frac{\partial u_i}{\partial x_j} &= -\delta_{i3}g + f\epsilon_{ij3}u_j - \frac{1}{\rho_a}\frac{\partial p}{\partial x_i} + v\frac{\partial^2 u_i}{\partial x_j^2}, \\
\frac{\partial \theta}{\partial t} + u_j\frac{\partial \theta}{\partial x_j} &= v_\theta\frac{\partial^2 \theta}{\partial x_j^2} - \frac{1}{\rho_a C_p}\frac{\partial Q_j^*}{\partial x_j} - \frac{L_p E}{\rho_a C_p}, \\
\frac{\partial q}{\partial t} + u_j\frac{\partial q}{\partial x_j} &= v_q\frac{\partial^2 q}{\partial x_j^2} + \frac{S_q}{\rho_a},
\end{aligned} \tag{1}$$

with the conserved quantities being the velocity vector components $(u_i = u, v, w)$, the potential temperature θ, and the specific humidity q. The air density is given as ρ_a, g is the gravitational acceleration, L_p denotes the latent heat of evaporation, C_p is the air specific heat at constant pressure, E is the heat released by phase changes, and $Q*$ is the divergence of net radiation. From left to right, these equations contain the terms of advection, pressure gradient force, the Coriolis force, and the (molecular) stresses with the molecular diffusivities for momentum, temperature, and humidity v, v_θ, and v_q, respectively. To include turbulent motion in the flow, the equations above are separated into a mean flow and a fluctuating part using the Reynolds decomposition

$$x = \bar{x} + x', \tag{2}$$

with x being one of each conserved quantity. Applying some averaging rules for the turbulent values and removing negligibly small terms gives the following set of equations.

$$\begin{aligned}
\frac{\partial \overline{u_j}}{\partial x_j} &= 0, \\
\frac{\partial \overline{u_i}}{\partial t} + \overline{u_j}\frac{\partial \overline{u_i}}{\partial x_j} &= -\delta_{i3}g + f\epsilon_{ij3}\overline{u_j} - \frac{1}{\overline{\rho_a}}\frac{\partial \bar{p}}{\partial x_i} + v\frac{\partial^2 \overline{u_i}}{\partial x_j^2} - \frac{\partial\left(\overline{u_i'u_j'}\right)}{\partial x_j}, \\
\frac{\partial \bar{\theta}}{\partial t} + \overline{u_j}\frac{\partial \bar{\theta}}{\partial x_j} &= v_\theta\frac{\partial^2 \bar{\theta}}{\partial x_j^2} - \frac{1}{\overline{\rho_a}C_p}\frac{\partial \overline{Q_j^*}}{\partial x_j} - \frac{L_p E}{\overline{\rho_a}C_p} - \frac{\partial\left(\overline{u_j'\theta'}\right)}{\partial x_j}, \\
\frac{\partial \bar{q}}{\partial t} + \overline{u_j}\frac{\partial \bar{q}}{\partial x_j} &= v_q\frac{\partial^2 \bar{q}}{\partial x_j^2} + \frac{S_q}{\overline{\rho_a}} - \frac{\partial\left(\overline{u_j'q'}\right)}{\partial x_j}.
\end{aligned} \tag{3}$$

These equations are similar to those in Equation 1 but are expressed in mean quantities. Furthermore, new divergence terms appear as $\overline{u_i'u_j'}$, $\overline{u_j'\theta'}$, and $\overline{u_j'q'}$.

Three major assumptions are made to Equation 3; 1) that only $j = 3$ ($u_3 = w$) is important, 2) horizontal homogeneity, where turbulent quantities do not change in x, y-direction ($\partial/\partial u_1 = 0$ & $\partial/\partial u_2 = 0$), and 3) steady-state, where quantities do not change in time ($\partial/\partial t = 0$) (Foken & Nappo, 2008).

The equations that follow after applying these assumptions still contain more unknown variables than there are equations. This gives rise to a *closure problem*. Near the surface, this problem is usually tackled using a *first order closure* or *K-theory* which relates the Reynolds covariances to the spatial gradient of the relevant mean quantity with the following equations:

$$\begin{aligned}\overline{u'w'} &= -K_m \frac{\partial \overline{u}}{\partial z},\\ \overline{w'\theta'} &= -K_h \frac{\partial \overline{\theta}}{\partial z},\\ \overline{w'q'} &= -K_q \frac{\partial \overline{q}}{\partial z},\end{aligned} \tag{4}$$

where K_m, K_h, and K_q are the turbulent diffusion coefficients for momentum, heat, and moisture in $[m^2 s^{-1}]$, respectively. The negative signs show that the turbulent diffusion acts in the opposite direction of the vertical gradient of the mean quantities. The eddy diffusion coefficients vary according to the static stability, being more efficient in unstable conditions and less efficient in stable conditions. The stability functions ϕ_m, ϕ_h, and ϕ_q are thus implemented to account for these differences. Including the stability parameter to the turbulent diffusion coefficients in Equation 4 gives

$$K_m = \frac{\kappa z u_*}{\phi_m}, \quad K_h = \frac{\kappa z u_*}{\phi_h}, \quad K_q = \frac{\kappa z u_*}{\phi_q}, \tag{5}$$

with the friction velocity $u_* = (\overline{u'w'}^2 + \overline{v'w'}^2)^{1/4}$ and the von Karman constant $k = 0.4$.

2.2 Flux-Gradient similarity

Fluxes are represented by their Reynolds covariances. The fluxes for sensible (Equation 6) and latent (Equation 7) heat are given as follows

$$Q_s = \rho_a c_p \overline{w'\theta'}, \tag{6}$$

$$Q_l = \rho_a L_s \overline{w'q'}, \tag{7}$$

with the air density ρ_a in $[kg\ m^{-3}]$, the air specific heat at constant pressure c_p in $[J\ kg^{-1} K^{-1}]$, the latent heat of sublimation L_s in $[J\ kg^{-1}]$, and $\overline{w'\theta'}$ and $\overline{w'q'}$ as the averaged covariances between the vertical velocity w and the conserved quantities potential temperature θ in $[K]$ and the specific humidity q in $[kg\ kg^{-1}]$. Throughout this work, the fluxes are defined as positive when directed away from the surface and negative when directed towards the surface.

The Monin-Obukhov (M-O) Similarity Theory can be used to describe the profiles of wind and temperature in the atmospheric surface layer. Under the assumption that fluxes are constant with height, the logarithmic profile of wind in the inertial sublayer is given as

$$\overline{u} = \frac{u_*}{\kappa} ln \frac{z}{z_0}. \tag{8}$$

Combining Equation 4 and Equation 5 for neutral stability gives the following equations for the Reynolds covariances

$$\begin{aligned} u_* = (-\overline{u'w'})^{1/2} = \kappa \cdot z \cdot \frac{\partial u}{\partial z} = \kappa \cdot \frac{\partial u}{\partial \ln z}, \\ \overline{w'T'} = -\kappa \cdot u_* \cdot \frac{1}{\mathrm{Pr}_t} \frac{\partial \theta}{\partial \ln z}, \\ \overline{w'q'} = -\kappa \cdot u_* \cdot \frac{1}{\mathrm{Sc}_t} \frac{\partial q}{\partial \ln z}. \end{aligned} \tag{9}$$

In these equations, Pr_t and Sc_t are the turbulent Prandtl and Schmidt numbers, respectively. They are introduced because the diffusion coefficients for momentum, sensible heat, and latent heat are not identical and are given by $\mathrm{Pr}_t = \frac{K_m}{K_h}$ and $\mathrm{Sc}_t = \frac{K_m}{K_E}$ (Foken & Nappo, 2008).

Integration of these equations between two heights gives the turbulent fluxes in the turbulent layer. Commonly, it is assumed that the surface values are identical to those at the bottom of the inertial sublayer. Thus, in addition to the surface temperature, only one measurement height is needed, and the integration is done from the surface (where $u = 0$) to the measurement height z.

After integration and including the stability parameters, the full equations for deriving the fluxes via the gradient method from the surface to height z are

$$Q_s = -C_s \overline{U} \rho_a c_p (\theta_z - \theta_0), \quad C_s = \frac{\left(\frac{K}{Pr}\right)^2}{\left[ln\left(\frac{z}{z_{0T}}\right) - \phi_T(\zeta)\right]\left[ln\left(\frac{z}{z_{0M}}\right) - \phi_M(\zeta)\right]}, \tag{10}$$

$$Q_l = -C_l \overline{U} \rho_a L_s (q_z - q_0), \quad C_l = \frac{\left(\frac{K}{Sc}\right)^2}{\left[ln\left(\frac{z}{z_{0q}}\right) - \phi_q(\zeta)\right]\left[ln\left(\frac{z}{z_{0M}}\right) - \phi_M(\zeta)\right]}. \tag{11}$$

The turbulent bulk exchange coefficients C_s and C_l depend on the stability parameter ζ, height z, the aerodynamic roughness length z_{0M}, and the turbulent Prandtl Pr and Schmidt Sc numbers, respectively.

2.3 Eddy covariance

Surface fluxes can be measured directly without any empirical constants using the eddy covariance (EC) method. This is done by using high-frequency measurements (10-20 Hz) of wind speed components, temperature, and water vapor to directly compute $\overline{w'\theta'}$ and $\overline{w'q'}$ in Equation 6 and Equation 7. Sonic anemometers measure time delays in the wind speed and temperature variables between opposing acoustic transducers. Temperature is measured by the speed of sound, and thus the measured temperature represents the virtual temperature. The humidity fluctuations are measured by a gas analyzer commonly placed next to the sonic anemometer. The same assumptions that were made at the beginning of this section still apply, i.e. there is no advection, the measurements are taken under steady-state conditions, there is horizontal homogeneity, and the fluxes are constant in the vertical. To use the EC method, many processing choices must be made. One of the important choices is the time-averaging interval, which is needed to take into account all eddy sizes contributing to the turbulent flux without including mesoscale motions. The second is the tilt correction method, which rotates the coordinate frame of the sonic anemometer to correct for any tilt in the instrument. Given that complex mountain terrain violates the assumptions described above, a thorough assessment of the choice of data processing is necessary. In the scientific community, no consensus has yet been reached on which post-processing techniques are best to use for turbulence data in complex terrain (Serafin et al., 2018).

3 Methods

In this section, we outline the data processing procedures and provide information about the model. First, we describe the measurement sites and the employed instrumentation and present a summary of the selected events chosen for analysis. Then, we state how we derive the turbulent heat fluxes from both high and low frequency data. Finally, we provide an overview of CRYOWRF, the model used to examine the spatial variability of the fluxes.

3.1 Measurement sites and instrumentation

Two field sites (GOT & WFJ) located in the mountains around Davos, Switzerland, are used to assess the performance of the model CRYOWRF. An overview map depicting the locations of these field sites and images of the instrument set-up are presented in Figure 1. Additionally, Table 2 provides detailed information about the instruments deployed at both stations.

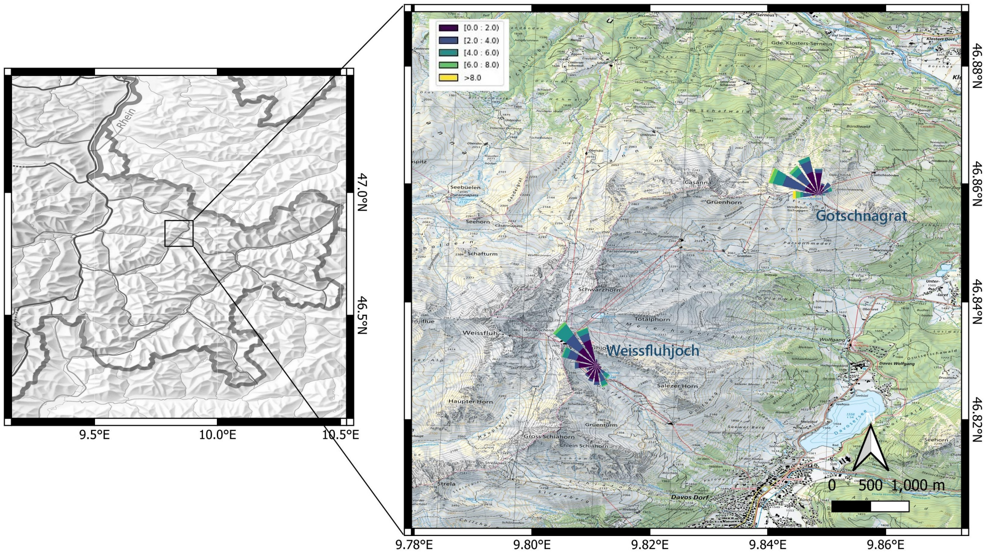

(a) Map of the Davos region in Switzerland. The wind roses show the locations of the stations of WFJ and GOT (GOT wind rose includes measurements from February - March 2019).

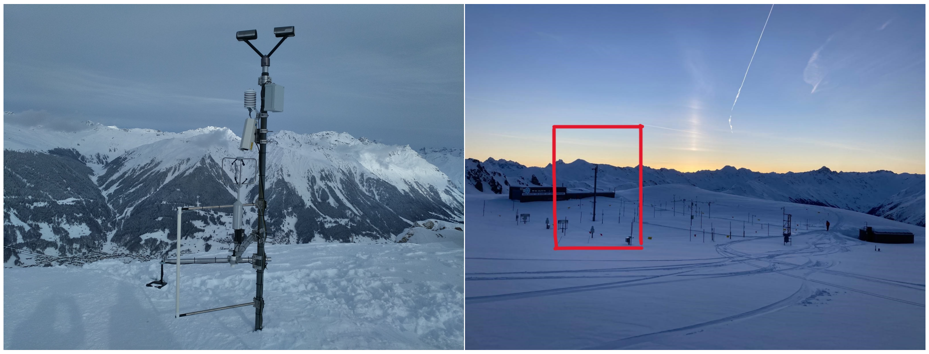

*(b) Instrument set-up at the **GOT** station. All available instruments are described in Table 2.*

*(c) The SLF versuchfeld including the eddy covariance mast in the red box at **WFJ**.*

Figure 1

3.1.1 Weissfluhjoch

The Weissfluhjoch (WFJ) station is located at the Snow and Avalanche Research field site at 2544 meters altitude in the Parsenn ski area. Three peaks surround this field site: Weissfluhjoch (2686m) to the north, Salezerhorn (2536m) to the southeast, and Schafläger (2681m) to the southwest. The research field itself is located on a flatter section on a south-east facing slope. On the research site, a Young RE-8500 sonic anemometer combined with a Li-COR 7500A gas analyzer is set up at a height of 3 m above snow-free ground. During the experiment, the effective height of the sensor above the surface varied between 95 cm and being partially buried in the snow depending on the snow height. The measuring frequency of the sonic anemometer and the Li-COR is 10 Hz. The research field site also contains an automatic weather station measuring temperature, wind speed, snow surface temperature, and reflected shortwave radiation. These measurements are used for the computation of fluxes using the Monin-Obukhov bulk method (further discussed in section 3.3.2). The predominant wind directions at Weissfluhjoch are either from the southeast or the northwest, which corresponds to up- and down-slope winds, respectively.

3.1.2 Gotschnagrat

The Gotschnagrat (GOT) field site is located 4.5 km northeast of the Weissfluhjoch field site. It is located slightly north of the Gotschnagrat ridge at 2280 meters altitude, next to the cable car station of Gotschnabahn. To the west lies Grüenhorn with an altitude of 2501 meters and to the northeast the terrain is a steep slope to Klosters. A Young RE-8500 sonic anemometer operated at 1.5 m above the snow cover from the 11^{th} of February until the 22^{nd} of March 2019 and measured fluctuations of wind and temperature with a frequency of 20 Hz. The GOT station does not include a gas analyzer. Along with the sonic anemometer, an air temperature sensor, relative humidity sensor, snow surface temperature sensor, and snow height sensor were installed (see Figure 1b). The predominant wind directions at the GOT station in the period of 11 February - 22 March are west, north, and east, with the wind from the south being completely blocked.

3.1.3 IMIS stations

Inter-Cantonal Measurement and Information System (IMIS) stations, owned by SLF, are situated at high-elevation locations to provide meteorological data for operational avalanche forecasts and warnings. There are 9 IMIS stations located within our smallest domain. We use this data for additional comparison between measurements and the model for 10 m wind speed, 2 m air temperature, and surface temperature. More information on these stations can be found in Lehning et al. (1999).

Variable	Instrument	Model	Height	Frequency
High-frequency wind & sonic temperature	Ultrasonic anemometer	Young 8100RE	3 m^a	10Hz
High-frequency water vapor	Gas analyzer	LI-7500A	3 m^a	10 Hz
Temperature	Temperature probe	Campbell T107	5 m^a	1 Hz
Wind	Wind Monitor	Young 05103	7.5 m^a	1Hz
Surface temperature	Infrarot radiometer	Campbell T107	5 m^a	1 Hz
Relative humidity	Humidity sensor	Rotronic Hygroclip	5 m^a	1 Hz
Snow height	Snow height sensor	Campbell SR50A	5 m^a	1 Hz
Shortwave radiation	Pyranometer	Campbell CS300	5 m^a	1 Hz

^{a} Above snow-free ground

Table 1: Variables, instrument names, instrument heights, and frequencies for the data at the ***Weissfluhjoch*** *station*

Variable	Instrument	Model	Height	Frequency
High-frequency wind & sonic temperature	Ultrasonic anemometer	Young 81000	1.5 m^b	20 Hz
Surface temperature	Infrarot radiometer	Campbell Sl-111	0.7 m^b	1 Hz
Relative humidity	Humidity sensor	Campbell CS-215	2.2 m^b	1 Hz
Snow height	Snow height sensor	Lufft SHM-31	1.7 m^b	1 Hz

^{b}Above snow surface on day 1

Table 2: Variables, instrument names, instrument heights, and frequencies for the data at the ***Gotschnagrat*** *station*

3.2 Event selection

To investigate the variability of turbulent fluxes depending on the synoptic flow, we choose three different weather patterns: a south föhn, a north föhn, and a calm day. Föhn is defined as a downslope wind induced by terrain characteristics that brings drier and warmer air to the lee side of the mountain range (Elvidge & Renfrew, 2016). This happens because ascending air cools and loses moisture through precipitation. The resulting dry air descends on the lee side of the mountain and warms with the dry adiabatic lapse rate. Davos is located on the north side of the main chain of the Alps. This means that during a south föhn event, Davos is on the lee side and affected by warm and dry descending air. Contrarily, during a north föhn event, Davos is on the windward side of the mountain chain and is supplied with moist, rising air which is usually combined with precipitation. By comparing flux measurements during these föhn events to those on a calm day, we aim to understand the spatial distribution of fluxes under varying meteorological conditions.

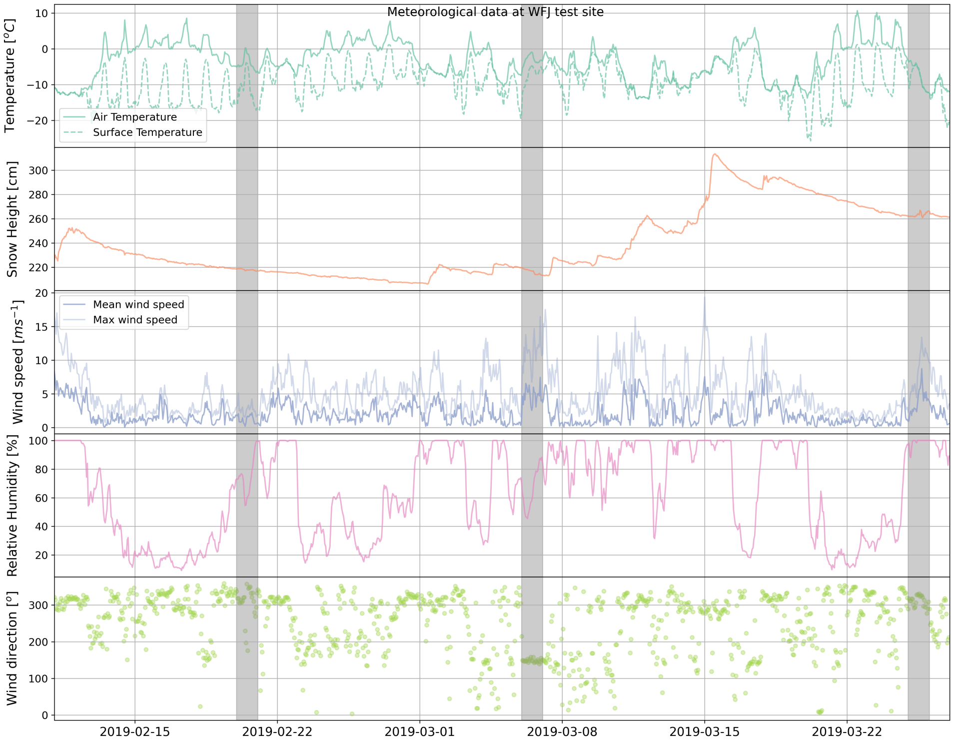

(a) Weissfluhjoch

(b) Gotschnagrat

Figure 2: Air and surface temperature, snow height, wind speed, relative humidity, and wind direction for Gotschnagrat and Weissfluhjoch during the measurement period. The grey bars denote the chosen events for the calm, south föhn, and north föhn events, respectively.

3.2.1 South föhn event

A south föhn event is defined with the following conditions at the Weissfluhjoch and Davos automatic weather stations (IMIS):

- constant wind direction from the south-west to south-east throughout the day,
- 30-minute average wind speeds exceeding 5 m/s,
- low relative humidity,
- increasing 2 m air temperatures during the event.

Additionally, the maximum air temperature of the day should not exceed $0\,^{\circ}\mathrm{C}$ at Weissfluhjoch as we wanted an event without surface melt of snow. Following these conditions, we chose the day of the 6^{th} of March. The synoptic scale pressure distribution was the following: a low-pressure system was present above the UK, which leads to a lower pressure at the north side of the Alpine ridge than at the south side. The wind follows the pressure gradient over the Alpine ridge from north to south (see Figure A.1a). On this day the snow height was 2.25 m at WFJ, meaning that the sonic anemometer was located only 0.75 m above ground.

3.2.2 North föhn event

We define a north föhn event when the Weissflujoch and Davos weather stations measure:

- predominant wind direction from the north,
- 30-minute average wind speeds exceeding 5 m/s,
- high relative humidity,
- decreasing 2 m air temperatures during the event.

Events with winds coming from the north are often accompanied by snowfall. Snow particles that pass through the sensor of the ultrasonic anemometer can influence the measurements by increasing the amount of spikes which makes the data unreliable. We chose an event that was not accompanied by snowfall for the analysis. Thre was no north föhn event that showed reliable data for both stations, therefore, we chose one event with only good-quality data from WFJ. This is the 25^{th} of March. Since the gas analyzer is even more sensitive to obstacles in the air, riming, and icing than the sonic anemometer, we had to discard gas analyzer data for WFJ on this day. Instead of obtaining sensible heat flux from eddy covariance, we computed the latent heat flux with the C-method (described in section 3.3.3). On this day a synoptic high-pressure system was located west of the UK and a low-pressure system above Scandinavia, the synoptic wind flows from north to south over the Alps (Figure A.1b). The snow height at WFJ was 2.6 m, meaning that the sonic anemometer was 0.4 m above the ground.

3.2.3 Calm event

The third event chosen is a calm event with mean wind speeds of less than 3 m/s. We selected the 20^{th} of February. There is no significant synoptic flow as the Alps lie in a high-pressure zone (Figure A.1c). On this day, the snow height is 2.2 m at WFJ, leading to a sonic anemometer sensor height of 0.8 m.

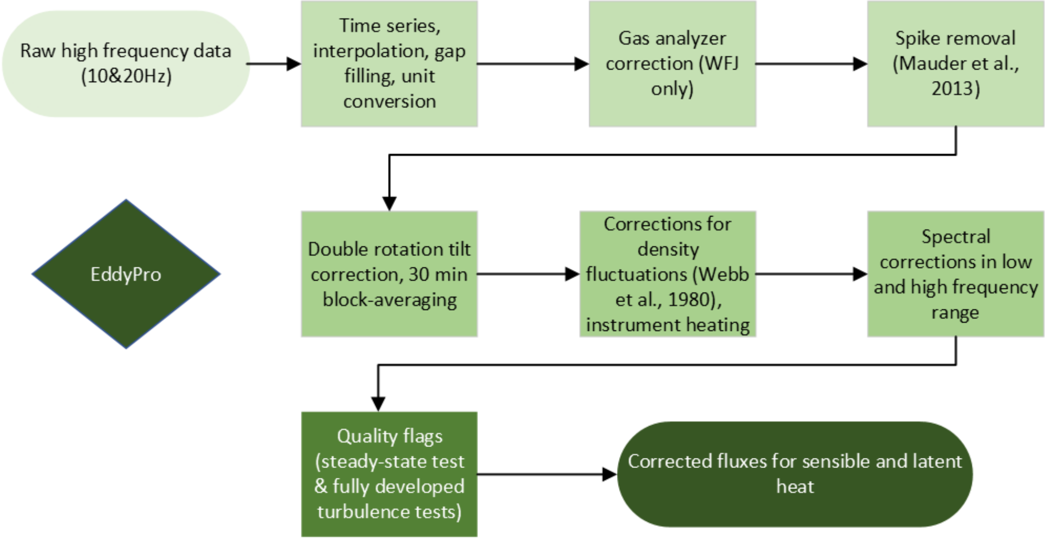

Figure 3: Flow chart of the data processing steps for the eddy covariance data.

3.3 Data processing

3.3.1 Eddy covariance method

We took various data-processing and quality-control steps to process the high-frequency eddy covariance data before computing the fluxes. Figure 3 gives an overview of all these steps. The first step of filtering the data is removing unphysical values from the dataset. Table 3 lists the plausibility limits that are applied and all data points falling out of these limits are removed.

	Ux $[ms^{-1}]$	Uy $[ms^{-1}]$	Uz $[ms^{-1}]$	Ts $[^oC]$
Lower limit	-40	-40	-10	20
Upper limit	40	40	10	-25

Table 3: Plausibility limits for data processing

We apply a water vapor correction to the gas analyzer data at WFJ. The calibration coefficients obtained are from the last calibration done in 2010. Its output is also calibrated against the relative humidity sensor of the IMIS station at the research site.

A limitation of the data from sonic anemometers is that they often exhibit large spikes during periods of snow, fog, or rain conditions due to distortion of the transducer pathways by particles. We use a spike removal algorithm as described in Sigmund et al. (2022) building on the algorithm proposed by Mauder et al. (2013). This algorithm uses the fact that spikes often occur simultaneously in the variables measured by the ultrasonic anemometer and most spikes occur as single-point spikes. The spike criterion relates the Median Absolute Deviation (MAD) of the conserved quantities

u, v, w, and T_{sonic} in a 5-minute rolling window to the standard deviation, as follows:

$$\frac{\hat{u}}{MAD(u)} + \frac{\hat{v}}{MAD(v)} + \frac{\hat{w}}{MAD(w)} + \frac{\hat{T}_{sonic}}{MAD(T_{sonic})} > \frac{q_s}{0.6745}, \tag{12}$$

with $q_s = 6$ being an empirical factor. Gas analyzer variables, such as water vapor, usually do not show spikes at the same time as the ultrasonic anemometer, so the spikes are removed independently using:

$$\frac{\hat{\rho_v}}{MAD(\rho_v)} > \frac{q_s}{0.6745}. \tag{13}$$

Next, we process the high-frequency data using the program EddyPro (LI-COR, 2021). An averaging window is chosen so that it takes into account all relevant eddy sizes which are dependent on location and stability conditions. We chose a block-averaging window of 30 minutes to compute turbulence as deviation from the mean flow as defined by Reynolds decomposition, without including large-scale fluctuations not related to turbulence.

Developments in turbulent flux computations show that a varying time-averaging window by Multi-resolution Flux Decomposition removes contamination by mesoscale motions and improves similarity relationships (Howell & Mahrt, 1997). This is especially true in stable conditions when turbulence time scales are small. To compare measured to modeled fluxes, applying this method will only result in a marginal gain and lies outside the scope of our research. We tested the difference between a 30-minute and 10-minute averaging window (given in Appendix B), which reveals a Mean Average Difference of $9.6\,\mathrm{W\,m^{-2}}$ for WFJ and $20.4\,\mathrm{W\,m^{-2}}$ for GOT. A similar study by Mott et al. (2011) showed that there are no significant differences in turbulent fluxes between a 30-minute and 15-minute time interval for the Weissfluhjoch test site. In our analysis, we adopt the same 30-minute averaging window as Mott et al. (2011). To filter out data of poor quality, averaging windows containing more than 40% missing values are excluded from flux computation.

The eddy covariance method requires a rotation of the coordinate system of the sonic anemometer for the wind measurements. This is done to correct for errors that may occur from a tilt of the sensor or misalignment and is especially important in complex terrain. Two tilt corrections are commonly used in micrometeorological analyses: the double rotation and the planar fit method. The double rotation method requires a rotation of the horizontal velocity u in the mean wind direction of the chosen averaging window to nullify cross-stream and vertical wind components. The first rotation is done around the z-axis and the second rotation around the y-axis. The rotation angles are calculated for every averaging period. The drawback of this tilt correction method is that when wind speeds are too low the coordinate system can be over-rotated. The first and second rotations are shown in Equation 14 and Equation 15, respectively. The subscript m denotes measured values in the reference frame of the sonic anemometer.

$$\begin{aligned} u_1 &= u_m cos\theta + v_m sin\theta \\ v_1 &= -u_m sin\theta + v_m cos\theta \\ w_1 &= w_m \\ \theta &= tan^{-1}\left(\frac{\overline{v_m}}{\overline{u_m}}\right) \end{aligned} \tag{14}$$

$$\begin{aligned} u_2 &= u_1 cos\phi + v_1 sin\phi \\ v_2 &= v_1 \\ w_2 &= -u_1 sin\phi + w_1 cos\phi \\ \phi &= tan^{-1}\left(\frac{\overline{w_1}}{\overline{u_1}}\right) \end{aligned} \tag{15}$$

In the planar fit method, introduced by Wilczak et al. (2001), the coordinate system of the sonic anemometer is rotated into the mean stream field of the wind as well, however, the mean stream field is determined over a longer time period (e.g., in our case 2 months of data). This tilted plane is determined by a least-squares regression on the entire dataset. The Z-coordinate is fixed over the chosen period.

We show the differences that arise from using these two tilt correction methods in Appendix B. The two methods show a Mean Absolute Difference of $6.9\,\mathrm{W\,m^{-2}}$ and $8.1\,\mathrm{W\,m^{-2}}$ at WFJ and GOT, respectively. Stiperski and Rotach (2016) found that these differences can be attributed to local advection induced by surface inhomogeneities in mountainous terrain. This could point to the influence of slope flows. The best tilt correction method is dependent on terrain characteristics and stability. During stable conditions in more complex terrain, the double rotation method showed the smallest scatter around the curve of best fit for σ_w/u_* vs. ζ in Stiperski and Rotach (2016). Thus, in further analysis of this work, we implement the double rotation method.

Additional corrections are incorporated by EddyPro, such as the correction for water vapor density fluctuations induced by fast changes in temperature fluctuations, defined by (Webb et al., 1980) and instrument heating defined by Burba et al. (2008). Spectral corrections in low and high-frequency ranges are applied by analytic correction of high-pass filtering effects (Moncrieff et al., 2004) and correction of low-pass filtering effects (Massman, 2000).

As a final step, we performed a quality control of the data. Quality flags are calculated for all heat fluxes as a result of tests described by Foken et al. (2004). These tests are based on the steady-state test and the fully developed turbulence conditions test. The fully developed turbulence test relies on the fact that the ratio between the standard deviation of a turbulent parameter and its turbulent flux remains nearly constant or varies as a function of stability (Thomas & Foken, 2002). The steady-state test determines the differences in covariances of meteorological variables within the time-averaging window, if these vary with more than 30%, there is no steady state (Foken & Wichura, 1996). For each test, a flag in the range of 0-1-2 is given, with

0 being a good-quality flux and 2 being of low quality. The flags for the tests are summed up and the fluxes with a quality flag of 2 are removed from the dataset.

3.3.2 Monin-Obukhov parametrization

In the absence of high-frequency wind, temperature, and water vapor measurements, turbulent fluxes can be computed using the Monin-Obukhov (M-O) similarity theory, a bulk method described in section 2.2. In this work, additionally to measuring turbulent fluxes directly with eddy covariance, we compute turbulent surface fluxes with the physics-based model SNOWPACK (Lehning et al., 2002). We force this model with meteorological data of air temperature, wind speed, relative humidity, and reflected shortwave radiation. The GOT station does not include a shortwave radiation sensor and thus we use the radiation measurements from WFJ for GOT. The heights of the instruments are given in Table 2. The SNOWPACK model solves Equation 10 and Equation 11, with the stability parameter computed as $\zeta = \left(-kz_{\mathrm{ref}}gT_*\right) / \left(\theta_s u_*^2\right)$.

In the flux computations by snowpack, we use similar parametrizations as implemented in the model CRYOWRF to be able to compare the two. For the stability correction, we use the expressions of ϕ by Holtslag and De Bruin (1988). This stability correction is one of the most widely used corrections and is recommended for very stable conditions (Andreas, 2002). The roughness length is set to $z_0 = 0.01\,m$. This roughness length lies between the values computed by Judith and Doorschot (2004) for WFJ, and typical roughness lengths for snow (Clifton et al., 2006).

3.3.3 Modified Bowen ratio/ C-method

At the GOT field site, no gas analyzer is present to measure the turbulent exchange of moisture. To compute the latent heat flux without the less reliable M-O theory parametrizations, we use a method first described by Businger (1986) as the modified Bowen-ratio method and revisited by González-Herrero et al. (2024) as the C-method. From the principle that turbulent eddies transport heat and moisture in the same way it is assumed that $C_l = C_s$. Starting from equation Equation 6, the latent heat flux is computed using the exchange coefficient from the sensible heat flux as follows:

$$Q_l = C_s \overline{\mathrm{U}} \rho_{\mathsf{air}}\, L_s \left(q_z - q_0\right) = \frac{\overline{w'\theta}}{\overline{\mathrm{U}}\left(\theta_z - \theta_0\right)} \overline{\mathrm{U}} \rho_{\mathsf{air}}\, L_s \left(q_z - q_0\right) = \frac{L_s}{c_p} \frac{\left(q_z - q_0\right)}{\left(\theta_z - \theta_0\right)} Q_s. \quad (16)$$

3.4 Model setup

To estimate the spatial variability of the turbulent heat fluxes, we use the model CRYOWRF. CRYOWRF is developed by the Snow and Avalanche Research Centre SLF and the EPFL Laboratory of Cryospheric Sciences and combines the atmospheric model Weather Research and Forecasting (WRF) with the surface model SNOWPACK (Sharma et al., 2021). WRF is a widely used, non-hydrostatic, and fully compressible model. The model is resolved on Eulerian mass dynamic cores.

CRYOWRF is set up with a vertical grid of 65 layers on terrain-following hydrostatic-pressure coordinates, extending up to 200 hPa. The timestep of the smallest domain is 0.06 seconds, which makes the run computationally expensive. Larger timesteps led to instabilities. For the output, data variables are averaged over 5-minute intervals. WRF allows for a wide choice of physics and dynamics options, including several different land-surface models, planetary boundary layer schemes, cloud microphysics schemes, and cumulus parameterizations. In this work, the boundary layer scheme is parametrized with the Yonsei University scheme (YSU) (Dudhia, 2010) for the first 4 domains, and domain 5 is run in Large Eddy Simulation (LES) mode. Mixing terms are evaluated in physical space and the sub-grid-scale turbulence is solved by the horizontal Smagorinsky first-order closure. At the same time, the vertical diffusion is taken care of by the boundary layer scheme.

We use a total of 5 nested domains to run the model. The first domain has a resolution of 27 km and a total grid size of 4000 km by 4000 km. The following domains have a smaller domain size and a resolution of 9 km, 3 km, 1 km, and 200 m, respectively. The boundary conditions and the input for the first time step are extracted from ERA-5 with a resolution of 27 km, equal to the first domain. This domain has a spin-up time of two days. Sequentially, the next domains start with boundary conditions given by the previous domain. For the smallest domain, we use a topography resolution by STMR with 1 arcsecond (National Geospatial-Intelligence Agency (NGA), 2000). A terrain smoothing option of 1-2-1 is applied a total of 6 times, which is needed to smooth slopes over 45^o.

The surface model in CRYOWRF, SNOWPACK, is a one-dimensional model that represents the snowpack at each grid point by a multi-layer column. SNOWPACK is able to split or merge snowpack layers based on density differences or similarities. The model solves the heat equation, together with snow compaction and water percolation. WRF provides the surface meteorological variables to the snowpack part of the model every 5 minutes. The surface turbulent heat fluxes are calculated by SNOWPACK and then returned to WRF.

CRYOWRF implements an additional blowing snow scheme as described by Sharma et al. (2021), which models the aeolian transport of snow particles, their sublimation, and re-deposition. The blowing snow model is a double-moment scheme that solves Eulerian advection-diffusion-type equations for the mass and number mixing ratios of blowing snow particles. This is done on an additional fine mesh grid between the surface layer and the first WRF layer. This scheme runs at every WRF timestep.

4 Results

The following sections present the results obtained from both measurements and the model. The first section contains a comparison of the point measurements of turbulent fluxes from both eddy covariance data and M-O data with modeled turbulent fluxes. Then, a section describes the model's performance in representing point measurements. In the final sections, we examine the results of the model, starting with the temporal evolution of cross-sections across the domain and then investigating specific topographical features and their influence on turbulent fluxes.

4.1 Point comparison of model and measurements

To assess the ability of CRYOWRF to represent locally measured turbulent fluxes, we compare measured fluxes at WFJ and GOT to the fluxes output by the model for three simulated days with different weather patterns: a south föhn, a north föhn, and a calm event. Additionally, we compare the model output for the fourth domain (resolution of 1 km) and the fifth domain (resolution of 200 m). The wind speed output for the model is at 10 m. To maintain consistency in wind speed height, we interpolate the wind speed from measurements to 10 m using the logarithmic wind profile, shown in Equation 8, which assumes neutrally stable conditions.

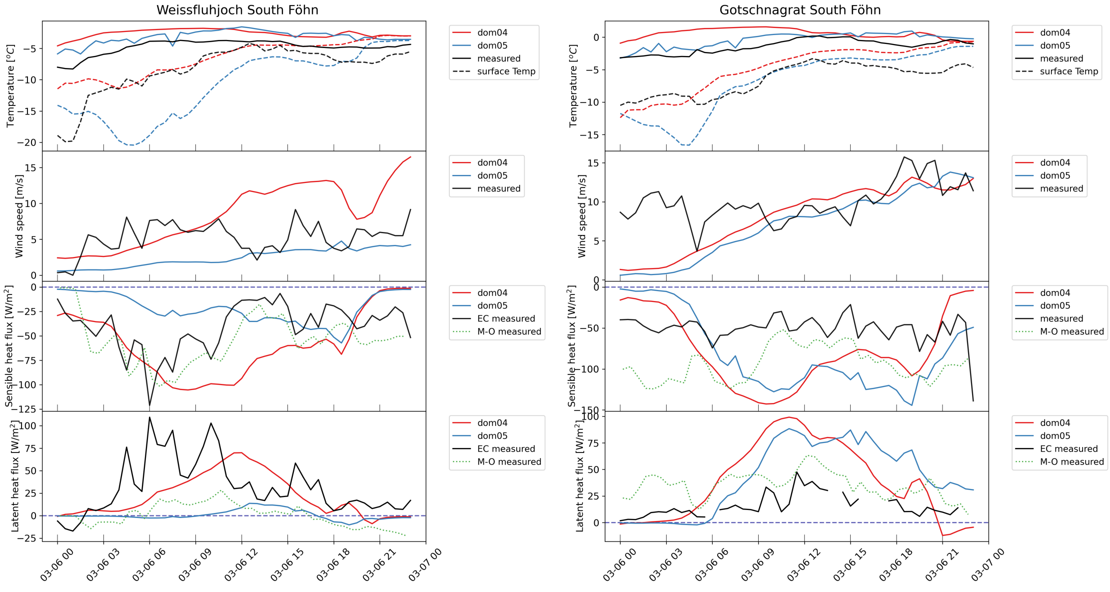

(a) *(b)*

Figure 4: Measured and modeled variables for air and surface temperature, wind speed, sensible heat flux, and latent heat flux for Weissfluhjoch (a) and Gotschnagrat (b) during the south föhn event. The black line shows measured values (eddy covariance method for the turbulent fluxes), the red line shows a coarse resolution (1 km), and the blue line shows a high resolution (200 m) domain. The dashed green line in the turbulent fluxes panel is the turbulent flux computed with Monin-Obukhov theory.

4.1.1 South föhn

High turbulent fluxes characterize the south föhn day. In Figure 4a, we present a time series illustrating both modeled and measured air and surface temperature, wind speed, sensible heat flux, and latent heat flux at the WFJ station. The significant temperature difference between the air and surface, driven by warm air carried over a cold surface by southerly winds, leads to a notable sensible heat flux towards the surface. The measured peak of the sensible heat flux, reaching -120 Wm^{-2}, occurs around 6:00. This high energy input to the snow cover subsequently leads to a decrease in air temperature difference between air and surface, which results in a smaller sensible heat flux. The bulk method for computing fluxes, depicted in the figure as a dashed green line, closely aligns with the direct measurements of sensible heat flux obtained via eddy covariance, shown by the black line.

The latent heat flux, measured by eddy covariance, shows a significant upward energy flux, reaching up to 100 Wm^{-2}, representing sublimation at the surface. During a south föhn event, on the northern side of the main Alpine ridge, the air tends to be dry. When this dry air is advected over the snow surface it results in a moisture gradient towards the air and sublimation occurs. The calculated latent heat flux by the bulk method is significantly smaller than that measured by the eddy covariance method. This disparity is partially attributed to the sublimation of blowing snow particles, a factor not accounted for by the bulk method. The M-O bulk parameterizations only account for exchange happening at the surface, not at the increased surface area caused by blowing snow particles (Sigmund et al., 2022).

Although model domain 4, represented by the red line in Figure 4a appears to reproduce turbulent fluxes adequately, this is primarily due to an underestimation of temperature difference at the start of the day and an overestimation of wind speed. Conversely, model domain 5 exhibits a very different evolution of the wind and temperature. The wind speed is underestimated leading to significantly lower fluxes compared to measurements. Due to the lower sensible heat flux, the temperature gradient between the surface and air does not decrease.

Figure 4b gives the time-series for the GOT station. Wind speeds observed are higher than those at WFJ, reaching values of up to 15 ms^{-1}. Surprisingly, despite the elevated wind speeds, the measured fluxes at GOT are approximately half the magnitude compared to WFJ. Moreover, fluxes measured by the bulk method surpass those measured by the EC method. The model, which uses M-O to compute fluxes, aligns more closely with M-O computed fluxes than EC measured fluxes. When M-O and EC data do not agree, it signifies that M-O is not valid to use in that situation. Reasons leading to EC and M-O differing are further discussed in section 5.5.2.

4.1.2 North föhn

Only data from the WFJ station is available for the North föhn event, as the data from the GOT station on this day was of too low quality. The latent heat flux for WFJ is computed with the Modified-Bowen ratio / C- method (section 3.3.3), as the gas analyzer produced too many spikes, attributed to the high moisture content of the air. The time-series is given in Figure 5. At this station, the air temperature decreases steadily throughout the day, while the surface temperature increases in the morning and decreases in the evening. Cloudy conditions prevent the surface from cooling significantly during the night due to high incoming longwave radiation. On average, the turbulent fluxes during this day are close to zero. During the night, both sensible and latent fluxes are negative, bringing heat and moisture to the surface. Cold air inflow from the north leads to surface temperatures to rise above air temperatures.

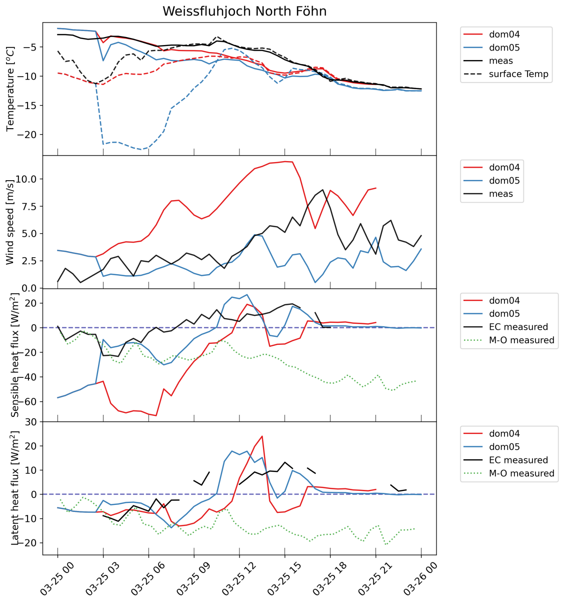

Figure 5: Measured and modeled variables for air and surface temperature, wind speed, sensible heat flux, and latent heat flux for Weissfluhjoch during the north föhn event. The black line shows measured values (eddy covariance method for the turbulent fluxes), the red line shows a coarse resolution (1 km), and the blue line shows a high resolution (200 m) domain. The dashed green line in the turbulent fluxes panel is the turbulent flux computed with Monin-Obukhov theory.

Subsequently, the sensible heat flux changes sign from negative to positive, resulting in a change of boundary layer stratification from stable to convective. Although the bulk method initially follows the trend observed by eddy covariance in the early morning, it deviates significantly after 6:00, failing to represent the sign change accurately. However, the model using the same bulk exchange method as M-O does capture this sign change in both domains. Slight differences between measured and modeled values of temperature result in these discrepancies, as the surface and air temperature lie close together. Similar to the south föhn event, the wind in domain 5 is underestimated, while the wind in domain 4 is overestimated. Despite this discrepancy, the fluxes do not exhibit significant differences between the domains.

4.1.3 Calm event

During the calm event (Figure 6), the two stations experience similar meteorological conditions. The air temperature remains constant throughout the day, while the surface temperature reaches its maximum at noon. Wind speeds reach their highest values in the morning and evening, peaking at $2.5\,ms^{-1}$, and dropping to $0.5\,ms^{-1}$ around noon. Both sensible and latent heat flux are low and negative in the morning and evening and reach a slight positive value up to $20\ Wm-2$ at midday. The low wind velocities translate into low turbulent fluxes. The marginal positive value in both fluxes in the measurements is likely due to heating of the surface by solar radiation, producing a weak convective boundary layer. The model domain 5 underestimates wind speeds for both stations, causing a slightly lower sensible heat flux and lower surface temperatures. The lower sensible heat flux also causes less heat transfer towards the surface which might cause discrepancies in surface temperature.

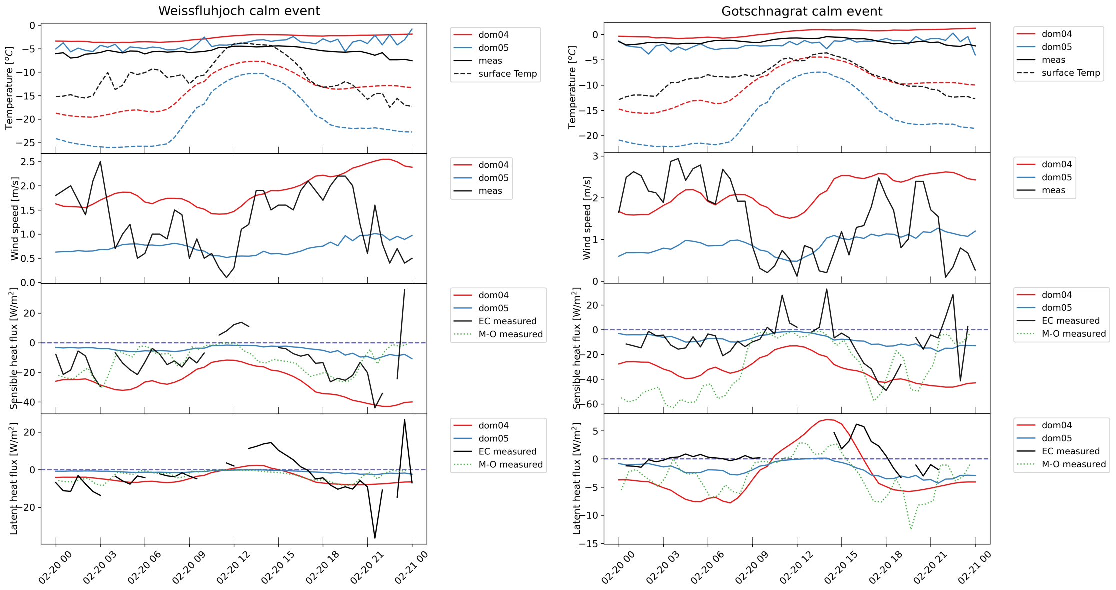

(a) *(b)*

Figure 6: Measured and modeled variables for air and surface temperature, wind speed, sensible heat flux, and latent heat flux for Weissfluhjoch (a) and Gotschnagrat (b) during the south calm event. The black line shows measured values (eddy covariance method for the turbulent fluxes), the red line shows a coarse resolution (1 km), and the blue line shows a high resolution (200 m) domain. The dashed green line in the turbulent fluxes panel is the turbulent flux measured with Monin-Obukhov.

4.2 Model performance

An overall comparison of the meteorological variables that influence turbulent fluxes provides insight into where the sources of error lie in the model for representing the turbulent fluxes locally. Specifically, 2 m air temperature, surface temperature, wind speed, and relative humidity are relevant. Table 4 offers an overview of the Mean Absolute Error (MAE) between measured and modeled variables for the different events. The computed air temperature exhibits an error ranging between 0.9 and 1.6 ^oC. Surface temperature, on the other hand, demonstrates a significantly larger deviation, reaching up to 8.8 ^oC. The wind speed has a mean absolute error between 0.7 to 3.0 ms^{-1}. These discrepancies in temperature and wind speed manifest in significant differences between sensible and latent heat fluxes obtained from measurements and the model. Notably, the difference can reach up to 43 Wm^{-2} for sensible heat during the south föhn event where the mean is -81 Wm^{-2} in the model.

These differences in the turbulent fluxes between the model and measurements are also evident from the scatter plot given in Figure 7. For sensible heat flux, the model underestimates the flux magnitude at Weissfluhjoch during the south föhn event, whereas it overestimates the flux at Gotschnagrat, this was also clearly seen in the time-series discussed in the previous section. Similar trends are observed for the latent heat flux. However, some uncertainties are also present within measured turbulent fluxes through the choices made in data processing, for example, tilt correction and time-averaging window (discussed in section 3.3.1 and shown in Appendix B).

	South WFJ	**South GOT**	**North WFJ**	**calm WFJ**	**calm GOT**
Air temperature $[^oC]$	1.7	0.9	1.1	1.6	1.1
Surface temperature $[^oC]$	3.9	2.1	4.6	8.9	7.6
Relative humidity $[\%]$	10.1	9.3	16.1	14.8	7.9
Wind speed $[ms^{-1}]$	1.8	3.0	2.0	0.7	0.8
Sensible heat flux $[Wm^{-2}]$	27.5	43.6	13.5	10.7	11.2
Latent heat flux $[Wm^{-2}]$	28.8	25.9	6.2	6.9	2.8

Table 4: Mean Absolute Error between modeled and measured variables per event and station.

This might further increase differences between model and measurements.

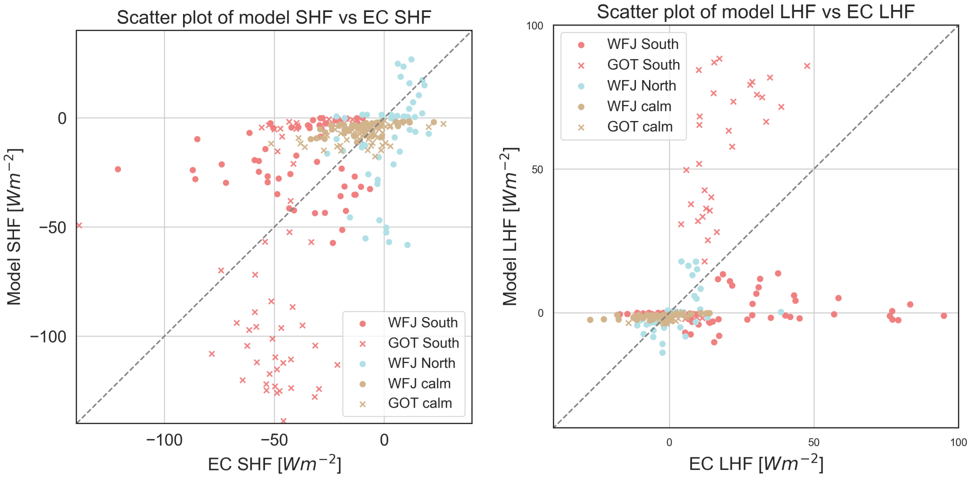

(a) Sensible heat flux

(b) Latent heat flux

Figure 7: Scatter plots of measured sensible heat flux (a) and latent heat flux (b) by eddy covariance versus the modeled turbulent flux from CRYOWRF for the three events for each station.

The IMIS stations located within the domain provide additional insights into the model performance in reproducing local predictions of meteorological variables, particularly 2 m temperature and 10 m wind. Figures displaying the comparison between model output and measurements for air and surface temperature, as well as wind speeds, are included in Appendix C. From the following time series of nine stations, the air temperature seems to be in the best agreement between the model and measurements. The surface temperature, which is not measured at every station, seems to be fairly accurate at some stations but varies substantially at others. The difference in modeled and measured wind speeds is much greater. This further highlights the limitation of the 200 m resolution to fully capture local variations in wind patterns.

It must be noted that the low resolution of the input data for snow height of 27 km produces large errors in snow depth at higher resolutions. The spin-up time of 2 days is not enough for the snow depth to melt out or accumulate to realistic values in certain locations. For example, in our smallest domain, there are still snow depths of more than 1 m in the low valley in the north of the domain with a minimum elevation of 600 m. This area is often snow-free in winter. For the computation of the sensible heat flux, the surface temperature plays an important role. As snow temperature can not rise above 0 ^{o}C, the temperature difference between surface and air is greater than in reality, and the sensible heat flux is overestimated. Similarly, the sublimation rates might differ due to differences in surface saturation. Henceforth, we will analyze the results assuming snow cover in these regions.

4.3 Cross sections

Two north-south cross-sections for the two föhn events, passing through the two measurement stations, along with the wind velocity field of the domain, are provided as animations in the electronic supplementary material. They can be found on the Youtube channel by clicking this link. In the animations, the top display illustrates potential temperature in height, the middle display depicts wind speed in height, and the bottom display shows the latent and sensible heat flux at the surface in Wm^{-2}. The blue line shows the location of Gotschnagrat and the red line the location of Weissfluhjoch.

The wind velocity field generally follows the synoptic wind patterns, but local topography strongly influences it. Orographic features create specific wind patterns, including cross-ridge flow with crest speedup and recirculation zones with low wind speeds on leeward slopes. These phenomena are evident, for instance, at 17:00 in the south föhn day in animation 1. Also, strong wind channeling in valleys, especially during thermally driven down-slope flows in the evening, occurs in the model and can be seen in the three valleys east of Davos, animation 5. From these animations, it becomes evident that the fluxes vary significantly in space and time depending on wind speed magnitude. The ridge where crest speed-up occurs has pertinent high turbulent fluxes, whereas the wind-sheltered leeward slopes do not. Additionally, the valley flows induce elevated turbulent fluxes.

In animation 1 which shows the south föhn day, the large valley located to the north of Gotschnagrat ridge contains a stably stratified cold-air-pool (CAP) during the day. When there are strong CAPs the air within the CAP is decoupled from the overlying air, which causes weak winds in the valley, and turbulence is also weak (Mahrt, 1999). Above the CAP, the advected air by the föhn can induce strong shear-induced turbulence, which can be seen by the difference between the low wind velocity in the CAP and the wind flowing above it. When the wind shear strengthens at the end of the day, it erodes the CAP, creating high turbulent fluxes in the valley. An additional animation of a planar view of the domain showing the variability of turbulent fluxes, in animation 5, further clarifies this.

Additionally, notable in animation 1 and animation 3 showing the south föhn event are the undulations observed in potential temperature and wind speed. These undulations can be interpreted as mountain-induced atmospheric gravity waves. Mountain waves typically form when an air mass, characterized by stable stratification, rises over a mountain range, generating buoyancy disturbances as it descends on the opposite side of the mountain (Doyle et al., 2002). They are most prominent when the boundary layer is highly stable, as is the case during the south föhn event. These waves manifest as alternating periods of high turbulence and calm periods. Kristianti et al. (2024) shows that mountain waves in the Alps can influence the atmosphere already at 100 meters above the surface. The animations provided reveal that higher surface wind speeds are observed where the wave trough reaches the surface, leading to increased and intermittent turbulence. This effect is particularly evident at the south-facing slope of the second peak viewed from the south. At 17:00 the wind velocity and the fluxes are close to zero, whereas two hours later at 19:00, the wind has strongly increased and the sensible heat flux reaches up to $-200\,Wm^{-2}$.

In animation 1 of the south föhn, the latent and sensible heat flux often mirror each other with opposite signs. This mirroring arises from differences between latent and sensible heat exchange processes. When air temperature increases and surface temperature stays constant, sensible heat flux increases in magnitude towards the surface (negative). Simultaneously, the air's capacity to hold moisture rises, leading to an increase in sublimation (positive). Contrarily, during fully saturated conditions, when deposition occurs, and if the surface temperature is still colder than the air temperature, energy transfer to the surface is positively correlated between sensible and latent heat. How the fluxes correlate, bringing energy to the surface can be seen in the night of the north föhn event in animation 2. In the morning, when air temperature drops below surface temperature, the sensible heat flux changes sign and the latent heat flux adopts the same switch. This negative correlation occurs because the water vapor gradient of the air closely follows the temperature gradient when the air is fully saturated. During midday of the north föhn event when sublimation occurs, the sensible and latent heat mirror each other again.

4.4 Spatial variability

In complex terrain, surface and air conditions vary significantly due to various topographical features. During synoptic weather patterns with winds coming from a specific direction, the slope aspect - whether on the windward or leeward side - influences air temperature and humidity. The angle of a slope can determine whether wind flows over or around the slope. Additionally, the elevation of a certain point influences the stability of the atmosphere and wind velocities (Mott et al., 2018). To understand the role of these topographical features on turbulent fluxes at a mountain scale level, we analyze changes throughout the day in sensible and latent heat fluxes that arise through differences in elevation, slope aspect, and slope angle.

4.4.1 Influence of elevation

Figure 8 shows the two turbulent fluxes per elevation bin, averaged over 24 hours per event for both sensible and latent heat. There are noticeable differences in variability across elevations among the events. During the south föhn event, the highest daily averaged sensible heat flux magnitude is observed at elevations ranging from 1900 to 2200 m, peaking at a mean of $30\,Wm^{-2}$ with a downward flux towards the surface. Conversely, the lowest daily average fluxes are observed at the lowest elevations of only $12\,Wm^{-2}$ despite the assumed snow coverage at these elevations. Regarding latent heat flux, the highest magnitude is observed around mid-elevations, specifically between 1600 and 1900 m, with $10\,Wm^{-2}$. In contrast to the south föhn, during the north föhn event, both sensible and latent heat fluxes exhibit a decrease in magnitude with increasing elevation. Sensible heat flux, on average, decreases to

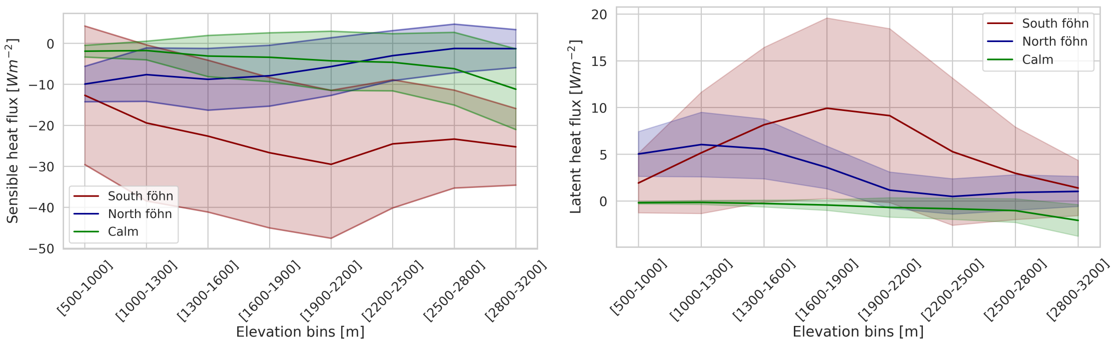

(a) *(b)*

Figure 8: Average of the sensible (a) and latent (b) heat flux for a whole day for each event per elevation bin. The dark line gives the mean of the elevation bin and the shaded area denotes the standard deviation.

values near zero at elevations of 2500 to 3200 m, mirroring the trend observed in latent heat flux. Opposite of the north föhn, the calm event shows an increase in the magnitude of both sensible and latent heat fluxes across elevation bins.

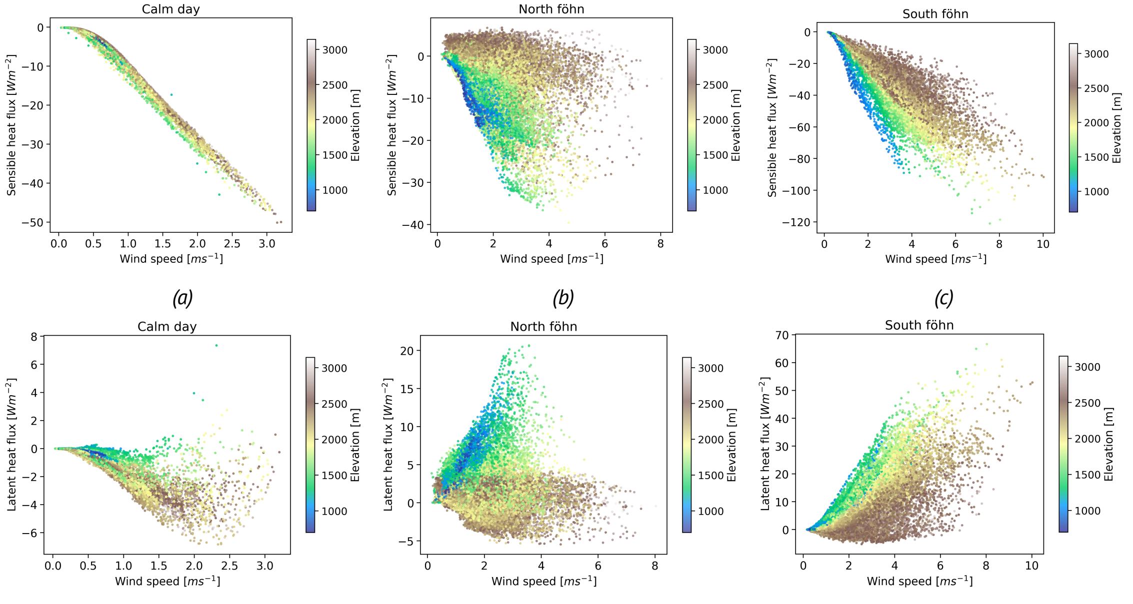

(a) *(b)* *(c)*

(d) *(e)* *(f)*

Figure 9: The relation between wind speed and turbulent flux for sensible heat in (a), (b), and (c), and latent heat in (d), (e), and (f) for each event. One scatter point represents the average value in 24 hours for one gridpoint. The color of the scatter point denotes the elevation in m of the gridpoint.

Figure 9 illustrates the relationship between wind speed and turbulent fluxes for the three events. Notably, the sensible heat flux exhibits a linear correlation with wind speed during the calm day. However, this linear relationship is not observed during either the south föhn and the north föhn days. Instead, these föhn days demonstrate an elevation-dependent relationship between wind and turbulent fluxes. The observed differences in these relationships can be attributed to the variability of surface and air temperature differences across different elevations for the föhn days.

To gain insight into both the spatial and temporal variability across different elevations which leads to the differences in the relation between wind and turbulent flux, we present plots depicting the sensible and latent heat flux per elevation bin throughout the day in Figure 10. The upper figures of Figure 10a, Figure 10c, and Figure 11a depict the mean flux per hour and the lower figures show the standard deviation within the elevation bin. To analyze the drivers of these variations, the most important meteorological variables for the fluxes through elevation and time are given in Figure 10b and Figure 11b. A high temporal and spatial variability can be observed when examining the turbulent fluxes per elevation bin throughout the day. Wind velocities are consistently the strongest at high elevations above 2800 meters across all events.

As depicted in Figure 10a, during the early morning, the highest magnitudes of sensible heat fluxes are present at the highest elevations, aligning with the presence of high wind velocities. However, by 12:00, a significant increase in sensible heat flux magnitude is observed at middle elevations (1300-2200 m), reaching a mean of $-50\,Wm^{-2}$. At night, the sensible heat flux counteracts radiative losses and lower elevations exhibit higher sensible heat fluxes than higher elevations, attributed to low differences between air and surface temperature at high elevations. In these high elevations, the surface temperatures are comparatively high at the end of the day due to the elevated sensible heat flux that was present during the day. Additionally, the air temperature decreases substantially in the evening due to decreased solar radiation, leading to low differences in surface and air temperature. In contrast, the lower elevations below 1000 m have significant magnitudes of sensible heat fluxes at the end of the day as a result of snow surface temperature remaining below 0 ^{o}C and air temperature rising. As already discussed in section 4.3, an increase in air temperatures arises when the föhn breaks through the stably stratified cold air pool at the bottom of the valley. This results in the sudden elevated wind speed and sensible heat fluxes after 20:00. It is important to note that in reality, the lowest elevations (500-1000 m) would not have a homogeneous snow cover, and surface temperatures would likely increase above $0^{o}C$, resulting in lower sensible heat fluxes and probably directed towards the air.

Regarding the latent heat flux, the highest daily averaged fluxes are observed in mid-elevations (1600-2200 m), reaching $10\,Wm^{-2}$. In contrast, the highest and lowest elevations exhibit the lowest sublimation rates, averaging $2\,Wm^{-2}$ and $1.5\,Wm^{-2}$, respectively. In Figure 10a a clear transition at the start of sunrise can be observed from deposition to sublimation. This sublimation is associated with increased air temperatures during a south föhn event which enables the atmosphere to hold more water vapor. Moreover, the dry air associated with the föhn enhances this effect. This transition happens earlier at mid-level elevations than at higher elevations, as mid-latitude air is a priori warmer. At higher elevations above 2200 m, the latent heat flux transitions back to deposition at 15:00, while at lower elevations sublimation stays throughout the evening. In this case at high elevations, surface and air temperatures are close to each other and as air temperature drops, the air which contains a lot of moisture due to the sublimation throughout the day, now reaches high relative humidity. This leads to deposition.

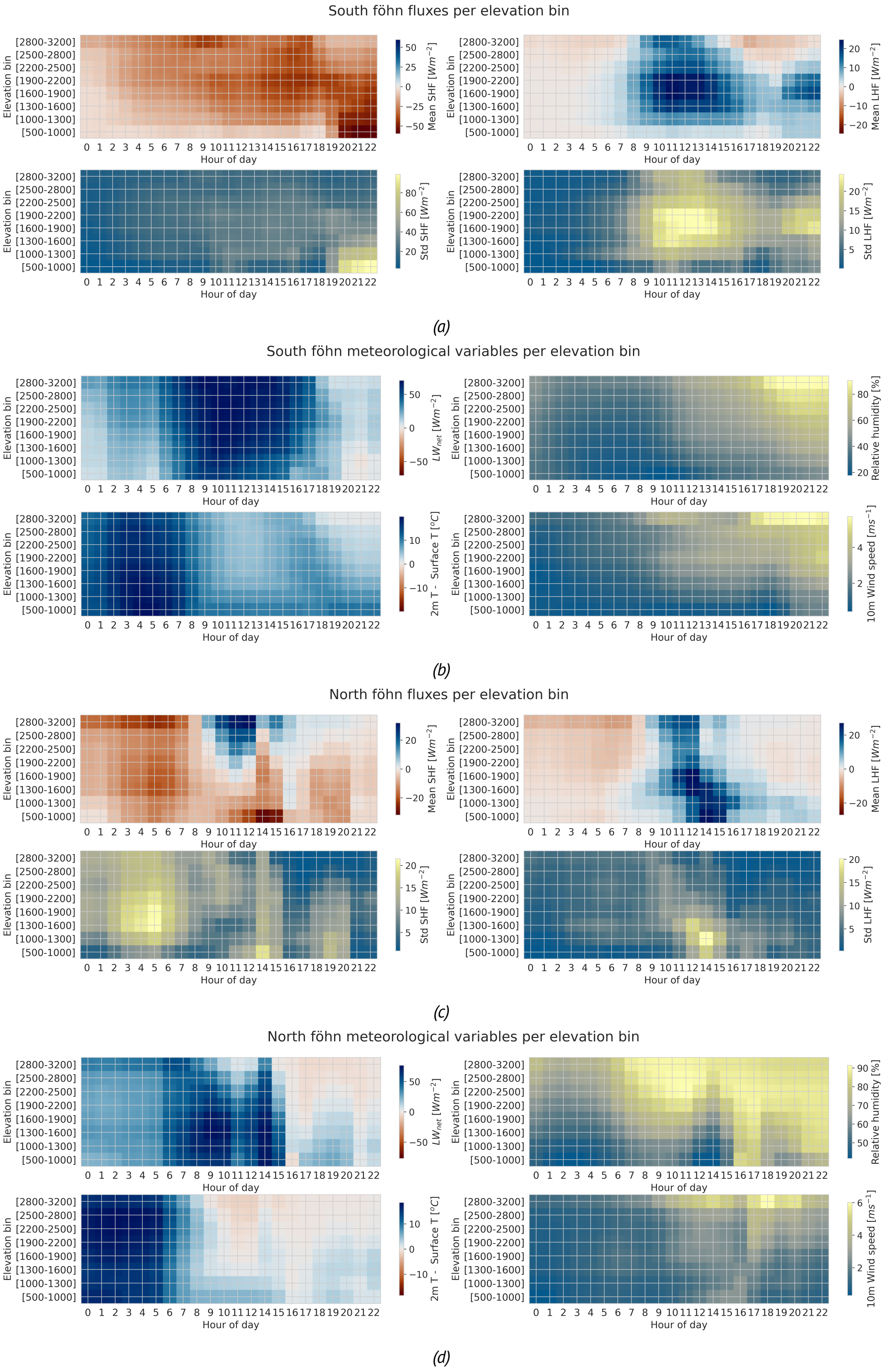

Figure 10: The hourly mean and standard deviation of the sensible and latent heat flux per hour of the day, per elevation bin for the south (a) and north föhn (c). Subfigures (b) and (d) give the meteorological variables that drive turbulent flux magnitudes for both events.

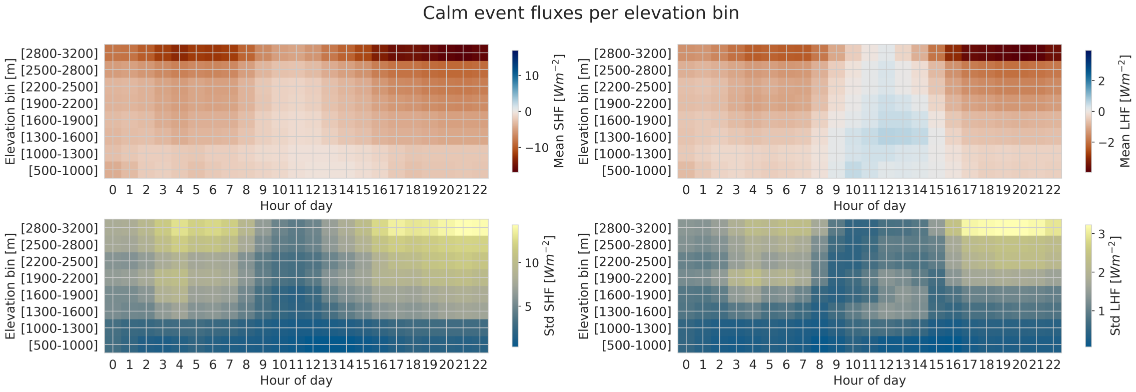

(a)

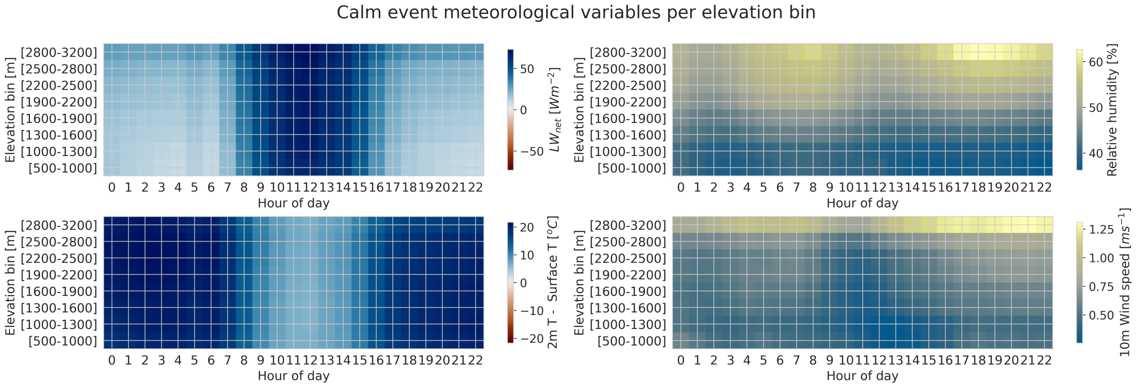

(b)

Figure 11: The hourly mean and standard deviation of the sensible and latent heat flux per hour of the day, per elevation bin for the calm day (a). Subfigure (b) gives the meteorological variables that drive turbulent flux magnitudes.

Looking at the variability throughout the day in the north föhn event in Figure 10c, the sensible heat flux is negative in the morning for all elevations. However, at elevations above 1800 m, the positive sensible heat flux cools the surface starting from 9:00 as air temperatures drop below surface temperatures due to colder advected air from the north. This wipes out the stable boundary layer and vertical mixing creates a convective boundary layer. At lower elevations, the local stable boundary layer and negative values of sensible heat flux persist. Similar to the south föhn event, the latent heat flux shows deposition in the night and sublimation during the day. However, at the end of the day, the mid-elevations of 1600-2500 m switch back to deposition, and elevations below 1300 m and above 2800 m still exhibit sublimation. This is the case as the latent heat flux adopts the same sign as the sensible heat flux when relative humidity is high.

Unlike the two föhn events described above, the calm day exhibits no significant variations in turbulent fluxes across elevations. In this event, the magnitudes of turbulent fluxes are greater at higher elevations compared to lower elevations, attributed to higher wind velocities at those altitudes, as observed in Figure 11a. Furthermore, the difference between surface temperature and air temperature, as well as the net longwave radiation, remains consistent across all elevations. This aligns with the results depicted in Figure 9, where the wind is the main driver for the magnitude of turbulent fluxes.

4.4.2 Influence of slope aspect and angle

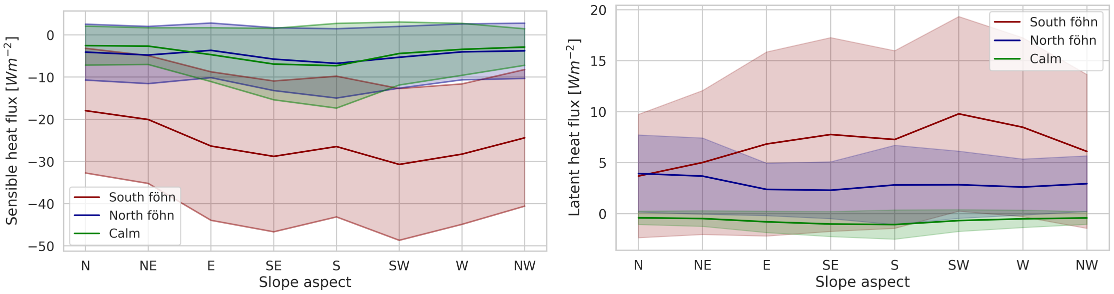

(a) *(b)*

Figure 12: Average of the sensible (a) and latent (b) heat flux for a whole day for each event per slope aspect bin. The dark line gives the mean of the slope angle bin and the shaded area denotes the standard deviation.

Figure 12 gives the daily average sensible and latent heat flux per slope aspect for the three different events. Additionally, Appendix D includes similar plots as those for elevation. The variability of turbulent fluxes across slope aspects is less pronounced than across elevation.

During the south föhn event, south-facing slopes exhibit a $5\,Wm^{-2}$ larger magnitude of negative sensible heat flux ($-29\,Wm^{-2}$) compared to north-facing slopes ($-24\,Wm^{-2}$) averaged over the whole domain for the whole day. The latent heat flux only shows a difference of $2\,Wm^{-2}$ from $7\,Wm^{-2}$ on south-facing slopes to $5\,Wm^{-2}$ on north-facing slopes. These differences can be attributed to stronger wind velocities and warmer air due to solar heating at south-facing slopes. The northern slopes are shadowed by solar radiation and southerly wind flows, which results in north-facing slopes having more deposition than sublimation due to colder and saturated air. The shadowing effect of the wind was also observed in the animations of section 4.3.

For the north föhn, the air temperature and sensible heat flux are greater in magnitude for south-facing slopes, also due to solar radiation. Surface temperatures do not differ significantly between the two slope aspects, and wind speed and latent heat flux are greater for north-facing slopes. This results in a mean sensible heat flux of north-facing slopes of $-4\,Wm^{-2}$ compared to $-6\,Wm^{-2}$ for south-facing slopes. The latent heat flux shows only very slight differences of $-2.8\,Wm^{-2}$ to $-2.1\,Wm^{-2}$.

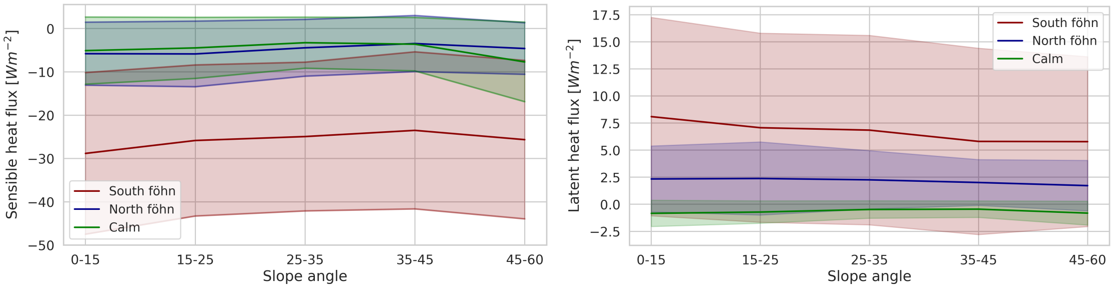

(a) *(b)*

Figure 13: Average of the sensible (a) and latent (b) heat flux for a whole day for each event per slope angle bin. The dark line gives the mean of the slope angle bin and the shaded area denotes the standard deviation.

Figure 13 presents the sensible and latent heat flux across slope angles as a daily average. Further details on the spatial and temporal variability of turbulent fluxes and meteorological variables, such as vertical wind velocity, horizontal wind velocity, the difference between surface and air temperature, and relative humidity across different slope angles, are shown in Appendix D. These figures reveal relatively consistent values for sensible and latent heat fluxes across various slope inclinations. Only marginally greater magnitude turbulent fluxes are found in less steep terrain. Part of this can be an artifact of the number of grid points per bin. The bin of 45-60 degrees contains fewer grid points than the other bins. In Appendix D, the only significant difference observed is in the vertical velocity, which leads to differences in advection by thermally driven slope flows.

5 Discussion

In this section, we first discuss the implications of the results and potential applications. Next, we examine how turbulent fluxes contribute to the overall energy balance across different events. Additionally, we investigate the significance of blowing snow sublimation to total sublimation. Following this, we assess the impact of resolution and the factors contributing to differences in modeled fluxes between 1 km and 200 m resolutions. Lastly, we discuss two limitations of the model: the selection of roughness length and the suitability of Monin-Obukhov similarity theory in complex terrain, and how these two factors may contribute to disparities between model predictions and measurements.

5.1 Spatial representation of turbulent fluxes

Mott et al. (2018) describe three scales at which processes happen that contribute to snow cover variability. These scales range from mountain range scale (kilometers to thousands of kilometers), to mountain-ridge scale (hundreds to thousands of meters), to slope scale (meters to hundreds of meters). The results we obtain from the model represent the processes happening on the mountain ridge scale, comprising the processes acting over the full length of a mountain ridge, including slope aspects and mountain crest. This is also the scale at which snow cover is shaped by preferential deposition (Lehning et al., 2008) and redistribution processes such as saltation and turbulent suspension.

Many hydrological models use spatially uniform melt rates applied to the basin snow water equivalent (Egli et al., 2012; Helbig et al., 2015). However, DeBeer and Pomeroy (2017) argue that this approach is not suitable for every topographic and climatic setting, and with increasingly complex terrain the spatial variability of near-surface wind velocities and turbulent fluxes vary by up to 20% from the mean. With this work, we also aim to demonstrate the importance of considering the spatial variability of turbulent fluxes for the computation of the energy balance of a snowpack in complex terrain. The previous results section highlighted these differences for individual weather patterns. Wind velocities play a major role in the variability of turbulent fluxes. Windward slopes, ridges, and valleys are subject to higher wind velocities and tend to have elevated turbulent fluxes compared to some leeward slopes.

Pohl et al. (2006) conducted a similar study on the spatial and temporal variability of turbulent fluxes in moderate complex terrain during snow melting periods. In that study, turbulent flux magnitudes were solely influenced by wind speed magnitude, consistent with our findings for the calm day. However, this linear correlation between turbulent flux magnitudes and wind speed magnitude is not consistently observed across all days. Elevation significantly influences air and surface temperature differences, as well as boundary layer dynamics, particularly during the two föhn events, leading to an elevation-dependent correlation between turbulent fluxes and wind speed. These results could serve as a foundation for developing a wind speed and elevation-dependent turbulent flux parameterization.

Regarding the two other topographical features influencing domain-wide differences in turbulent flux magnitude, namely slope aspect and angle, we observed their lower impact on a mountain ridge scale. However, looking at solely the slope scale, these features could lead to more pronounced differences, primarily due to wind effects. Slope aspect achieves this by sheltering leeward slopes from the wind and causing variations in incoming solar radiation, although dependent on surrounding topography. Meanwhile, slope angle influences turbulent fluxes through variations in wind velocities and vertical transport induced by thermally driven slope flows. This suggests that when developing a parametrization for turbulent fluxes, elevation should be a primary consideration, as a wind-dependent parametrization would encompass variations resulting from slope aspect and angle.

Beyond the aforementioned hydrological models, the results of this study are also relevant to avalanche forecasting, where an understanding of the energy input is crucial for assessing the development or destabilization of weak layers. Considering differences due to elevation can be critical.

5.2 Energy balance

In snow-covered areas during winter, turbulent fluxes of latent and sensible heat are typically small due to turbulence damping in stable conditions and the low availability of energy. However, during periods characterized by high wind velocities and when melting occurs, these fluxes can significantly contribute to the total energy balance, at times constituting up to 50% (Schlögl et al., 2017).

In Figure 14, we show the magnitude of the four main components of the energy budget for the snowpack for our case studies. The total energy budget is given in the following equation:

$$E = Q_S + Q_L + Q_h + Q_e + Q_G + Q_P, \tag{17}$$

where Q_S is the net shortwave radiation, Q_L is the net longwave radiation, Q_h is the sensible heat flux, Q_e is the latent heat flux, Q_G is the ground heat flux, and Q_P is the energy from precipitation. In our analysis, we disregard Q_P due to the absence of precipitation, and Q_G due to its negligible influence on snow melt at the surface.

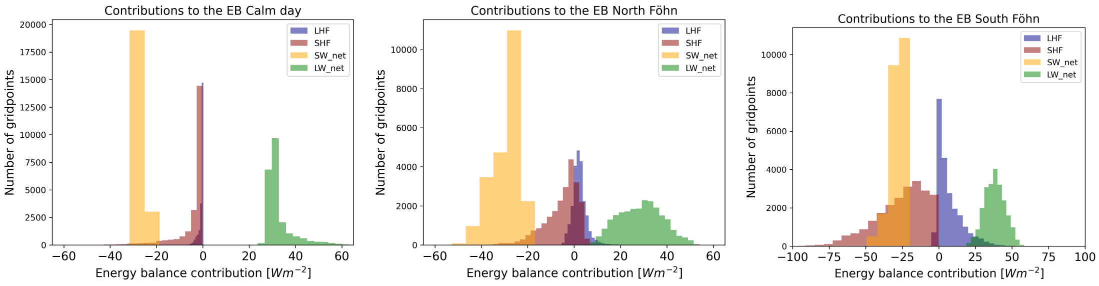

(a) *(b)* *(c)*

Figure 14: The four main contributors to the energy balance which are net longwave (LW_{net}), net shortwave (SW_{net}), sensible (SHF), and latent (LHF) heat flux, as average throughout the day for the calm (a), north föhn (b), and south föhn (c) days. The y-axis gives the number of grid points with a certain value of energy in $\mathrm{W\,m^{-2}}$.

Figure 14 shows the distribution of the daily average of four major contributors to the surface energy balance of a snowpack for all three events. On the calm day, the two turbulent fluxes are an order of magnitude lower than the two radiative fluxes, with median values near zero. However, on the north föhn day, variability among energy components increases, and sensible and latent heat fluxes approach average radiative flux values. In the south föhn day, the median of the sensible heat flux is close to the median of the net shortwave radiation, and even surpasses this in some grid points with double the magnitude.

This shows that the contribution of the turbulent fluxes to the total energy balance is dependent on the synoptic weather pattern. At times, these fluxes can exert a significant influence, even surpassing the magnitude of shortwave and longwave radiation on a daily average. Generally, the sensible heat flux tends to exhibit higher values compared to the latent heat flux. However, sublimation of snow also plays a significant role in the mass balance of the snowpack, as elaborated in the following section.

5.3 Blowing snow sublimation

Sublimation is an important part of the mass balance of a snowpack. During events with high wind velocities, total sublimation rates can increase due to sublimation of drifting and blowing snow particles (Pomeroy & Essery, 1999; Sigmund et al., 2022). Consequently, enhanced sublimation of snow particles contributes to an increase in relative humidity and cooling of the air. This, in turn, can lead to reduced surface sublimation, creating a feedback loop in the sublimation process.

In CRYOWRF, sublimation on the surface and sublimation of blowing and drifting snow are calculated separately. Sublimation from blowing snow is computed on both the fine mesh grid and the WRF vertical grid at every WRF timestep. The total mass loss due to surface sublimation per event can be quantified and is compared to the total sublimation in $\mathrm{kg\,m^{-2}}$. During the two föhn events, blowing snow is present throughout the whole domain. However, sublimation is concentrated in only part of the domain with the highest blowing snow amount. The figures below (Figure 15), which depict the average blowing snow sublimation over the full day of the south and north föhn events, show the local character of blowing snow sublimation.

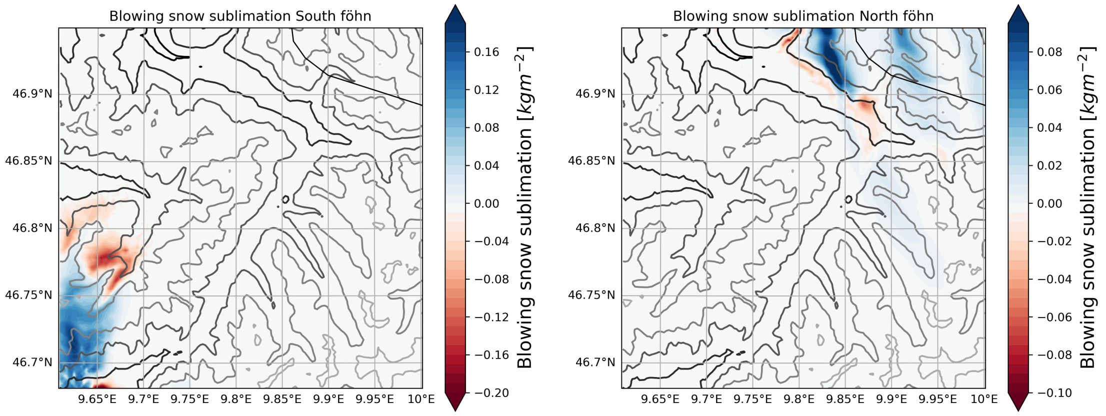

(a) *(b)*

Figure 15: Sublimation only from blowing snow averaged over the whole day for the south föhn (a) and north föhn (b) event in kgm^{-2}.

The mass loss due to surface sublimation and drifting and blowing snow sublimation per elevation bin is given in the figure below (Figure 16). Note the difference in magnitude of the y-axis in the histograms, the domain-averaged sublimation by blowing snow is an order of magnitude lower than sublimation from the surface.

Blowing snow sublimation shows locally a similar magnitude to total sublimation, with a maximum of $0.15\,\mathrm{kg\,m^{-2}}$ for the south föhn day in the lower left domain corner and $0.1\,\mathrm{kg\,m^{-2}}$for the north föhn day in the upper right domain corner. However, elevation averaged the maximum magnitude is $0.01\,\mathrm{kg\,m^{-2}}$. In both cases, blowing snow redeposition occurs on the leeward side of where the sublimation occurs. There is no clear elevation dependence in blowing snow sublimation. In both cases, the lowest and highest elevations have the least blowing snow sublimation, however, this can be an artifact of the small number of grid points in these elevation bins.

While previous studies, such as Vionnet et al. (2014) and Strasser et al. (2008), have highlighted the significant influence of blowing snow sublimation on total sublimation, our case studies present contrasting results. For instance, Vionnet et al. (2014) simulated a day at Col du Lac Blanc in the French Alps and reported that total sublimation is three times higher when blowing snow is considered, compared to when it is not. In our case studies, the contributions of drifting and blowing snow sublimation to total sublimation are found to be very local and relatively low when averaged domain wide. This is in line with a study of Groot Zwaaftink et al. (2013) which found that the contribution of blowing snow sublimation is very small on a seasonal time scale, but can be significant locally and on short timescales. The study of Groot Zwaaftink et al. (2013) was conducted in the Wannengrat area with $2.4\,\mathrm{km}^2$ and $10\,\mathrm{m}$ resolution located inside our smallest domain. Consequently, disregarding the blowing snow sublimation for our events would not markedly impact the total sublimation for longer time periods.

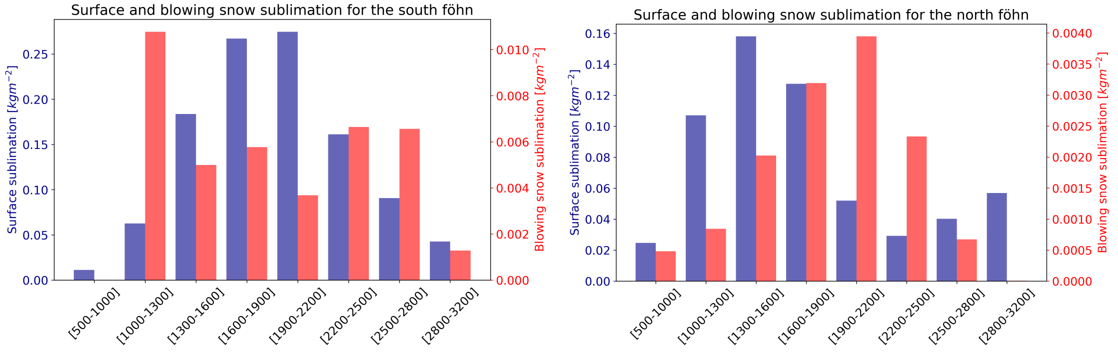

(a) *(b)*

Figure 16: Mass loss due to surface sublimation (blue) and blowing snow sublimation (red) in kgm^{-2} per elevation bin for the south föhn (a) and north föhn (b) event.

5.4 Effect of resolution

To assess the influence of model resolution on our results, we compare the differences in turbulent fluxes between 1 km and 200 m resolutions. As previously discussed in section 4.1, higher resolution simulations generally exhibit lower wind speeds compared to coarser resolutions, which translate into differences in modeled fluxes.

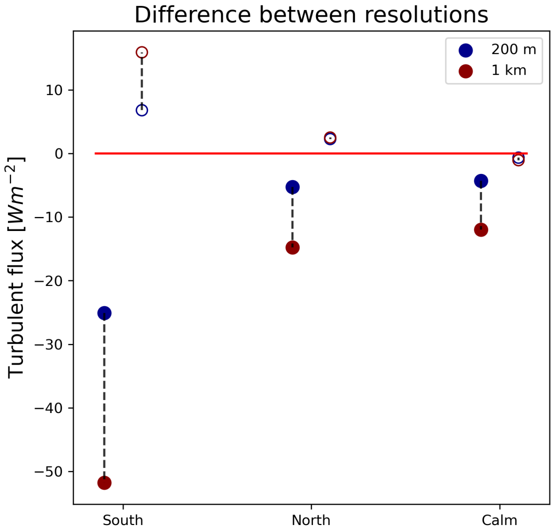

Figure 17: Sensible and latent heat flux averaged over the whole domain and over a full day (24 hours), for both domain 5 (blue) and domain 4 (red). The filled dots represent the sensible heat flux and the open dots represent the latent heat flux.

Looking at the average turbulent heat flux for both domains in Figure 17 for each event, we observe large differences. The sensible heat flux varies up to double the magnitude per resolution. This discrepancy can be attributed, at least in part, to the smoother representation of topography in coarser resolutions, resulting in reduced topography-wind interactions and subsequently higher wind speeds. The apparent differences in wind speeds between resolutions are evident in Figure 18, wherein the coarser (1 km) resolution consistently depicts markedly higher wind speeds, particularly noticeable in high elevation regions. These discrepancies underscore the impact of well-resolved topography on modeled fluxes, suggesting that higher resolutions can substantially improve estimations.

Moreover, the 200 m resolution domain operates in Large Eddy Simulation (LES) mode, whereas the 1 km resolution does not. In LES mode, the model directly resolves eddies, whereas non-LES mode relies on parameterizations for sub-grid scale turbulence. With the current simulations, we can not state if any differences arise due to these different ways of resolving the boundary layer. A 200 m resolution is within the grey area for LES usage, capable of resolving eddies only down to 200 m. Such large eddies are typically encountered in convective boundary layers, whereas turbulent eddies in stable boundary layers tend to be considerably smaller.

5.5 Limitations of the model

The results of the point comparison between the model and direct measurements of turbulent fluxes reveal substantial deviations. One contributing factor to these disparities is the challenge of precisely capturing the wind field when interpolating to a single point. While the model provides a broad representation of wind patterns, it does not capture fine-scale topographical features at a 200 m resolution. These unaccounted-for features can significantly influence the wind field at individual points, leading to discrepancies in wind velocities. Consequently, these differences

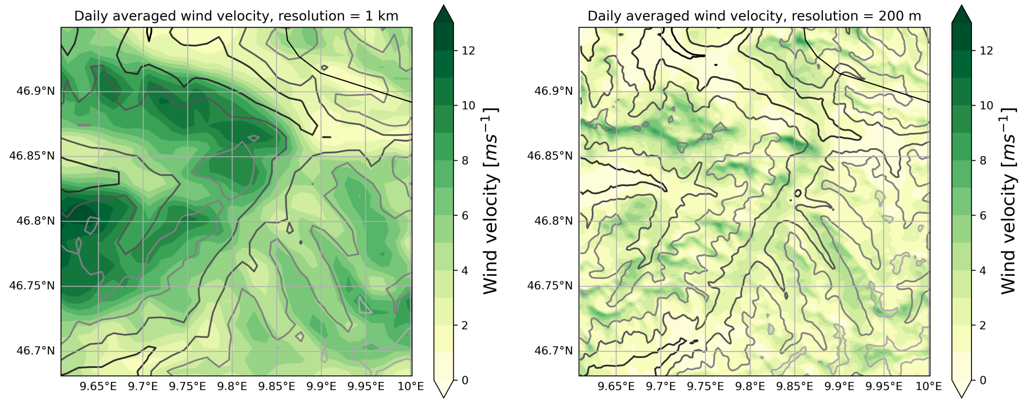

(a) *(b)*

Figure 18: Daily average wind velocity on the south föhn day for the 1 km resolution (a) and 200 m resolution (b). The coarser resolution shows significantly higher and more homogeneous wind velocities than the higher resolution domain.

in wind speeds contribute to differences in turbulent fluxes observed between the model and direct measurements.

However, as first observed in section 4.1.1 for the GOT station, the wind field is reasonably well resolved, yet deviations persist between the fluxes measured directly with eddy covariance and those modeled. Moreover, even fluxes indirectly computed using M-O theory from station data sometimes exhibit differences from the eddy covariance-derived fluxes.

The next two subsections discuss further limitations of using Monin-Obukhov in complex terrain and how these limitations can lead to differences between the model and measurements.

5.5.1 Roughness length

The roughness length z_0 is an important parameter in turbulent flux computations applied within M-O. How it is implemented in the equation can be seen in Equation 10 and Equation 11. CRYOWRF adopts a fixed roughness length over snow-covered areas, setting $z_0 = 0.01\,\mathrm{m}$, regardless of terrain complexity. To compare the model roughness length with that computed from high-frequency sonic anemometer data for both stations, we initially solved Equation 8 and took the median value. This involves applying a strong selection criterion for $u*$ to remove values of high $\frac{\sigma_w}{u*}$. The result gives a roughness length of $0.032\,\mathrm{m}$ for WFJ, including 635 measurements, and $0.015\,\mathrm{m}$ for GOT, including 225 measurements. Given the variability in wind measurement height over the observation period due to fluctuating snow depths, the measurement height is taken as a mean over the measurement period.

González-Herrero et al. (2024) argues that using a method described by Panofsky (1984) to compute the roughness length yields better results, as this method considers integral turbulence characteristics. The computation is as follows:

$$z_0 = z/exp\left(1.25\kappa\frac{\overline{U}}{\sigma_w}\right), \tag{18}$$

with σ_w being the standard deviation of the horizontal wind velocity. This method yields half the magnitude of values obtained from the logarithmic wind profile approach. The roughness lengths with this method are $z_0 = 0.013\,\mathrm{m}$ for WFJ and $z_0 = 0.0073\,\mathrm{m}$ for GOT.

The difference between the roughness length computed from station data and the roughness length adopted in CRYOWRF can influence the accuracy of the model to represent real turbulent fluxes. A higher value for roughness length leads to more elevated fluxes. The roughness length computed with the method of Panofsky (1984) for GOT is lower than the one implemented in the model and used for the M-O computation with station data, which could partially explain the overestimation of fluxes with M-O (section 19b)). Moreover, the roughness length can depend on wind direction in heterogeneous terrain (Panofsky, 1984), which poses an additional challenge.

5.5.2 Applicability of Monin-Obukhov

A dedicated section should be allocated to discussing the applicability of the Monin-Obukhov theory in estimating turbulent fluxes within complex terrain. Although M-O theory remains commonly used in such contexts, recent studies have questioned its suitability for accurately determining fluxes in complex terrain, as it violates the main assumptions of horizontal homogeneity, stationarity, and approximate constant fluxes in the vertical (Foken, 2006; Stiperski & Calaf, 2018). Stiperski and Calaf (2023) proposed an adapted version of the Monin-Obukhov similarity theory incorporating turbulence anisotropy as an additional non-dimensional term.

When significant discrepancies arise between fluxes computed by eddy covariance and those predicted by M-O theory, it indicates that M-O might not be accurate in representing these fluxes. Consequently, models employing M-O are likely to perform poorly in such cases, for instance in the south föhn event of Gotschnagrat and the north föhn event at Weissfluhjoch (Figure 4b, Figure 6a). In the cases where fluxes derived from M-O and eddy covariance exhibit notable disparities, applying a three-layer model (3LM) improves turbulent flux estimations using a bulk method. This 3LM is described by Sodemann and Foken (2005) and introduces an additional layer between the surface (z_0) and the measurement height (z),

With increasing stability of the lower atmosphere, the layers can become decoupled. Also, during katabatic winds over a rough surface, a roughness sublayer may develop below the inertial sublayer. A characteristic of katabatic winds is a wind speed maximum close to the surface. At the wind speed maximum, the generation of turbulence by shear is zero, as well as the vertical exchange of momentum. By definition, the friction velocity and the Obukhov length will also be zero. This can lead to a total decoupling of the flow (Denby, 1999).

When there are excessive gradients in the molecular and buffer layer computing M-O between the surface values and the values at a certain height z is not valid. The M-O bulk method then uses a gradient that is too large, and this leads to an overestimation of the turbulent fluxes. Using a 3LM can improve estimations of fluxes in this case. The sensible heat flux from the 3LM can be determined by the following equation

$$Q_s = \Gamma \rho_{air} c_p \left[T_0 - T_z \right], \quad \Gamma = \frac{\kappa \cdot u_*}{(\kappa \cdot \mathrm{Pr} - 1/6) \cdot \delta_T^+ + 5 + \ln \frac{u_{*'} z}{30\nu}}, \tag{19}$$

where $\nu = 1.461 \times 10^{-5}\,\mathrm{m\,s^{-1}}$ is the kinematic viscosity and δ_T^+ is a dimensionless temperature difference in the buffer layer, with

$$\frac{\delta_T u_*}{v} = \begin{cases} 6, u_* \leq 0.23\,\mathrm{m\,s^{-1}} \\ 12, u_* > 0.23\,\mathrm{m\,s^{-1}} \end{cases} . \tag{20}$$

Figure 19 below depicts a comparison of the 3LM, M-O, and EC methods for the north and south föhn event. The 3LM shows no significant improvement during the highly stable event of the south föhn. However, during the north föhn event, where M-O fluxes notably differ from EC, the 3LM effectively represents fluxes. This strong discrepancy between M-O and the two other methods, EC and 3LM, during the north föhn suggests a strong gradient in the buffer layer. Additionally, the 3LM can not be subject to wrong estimations of roughness length, as it is not included in the equations (González-Herrero et al., 2024).

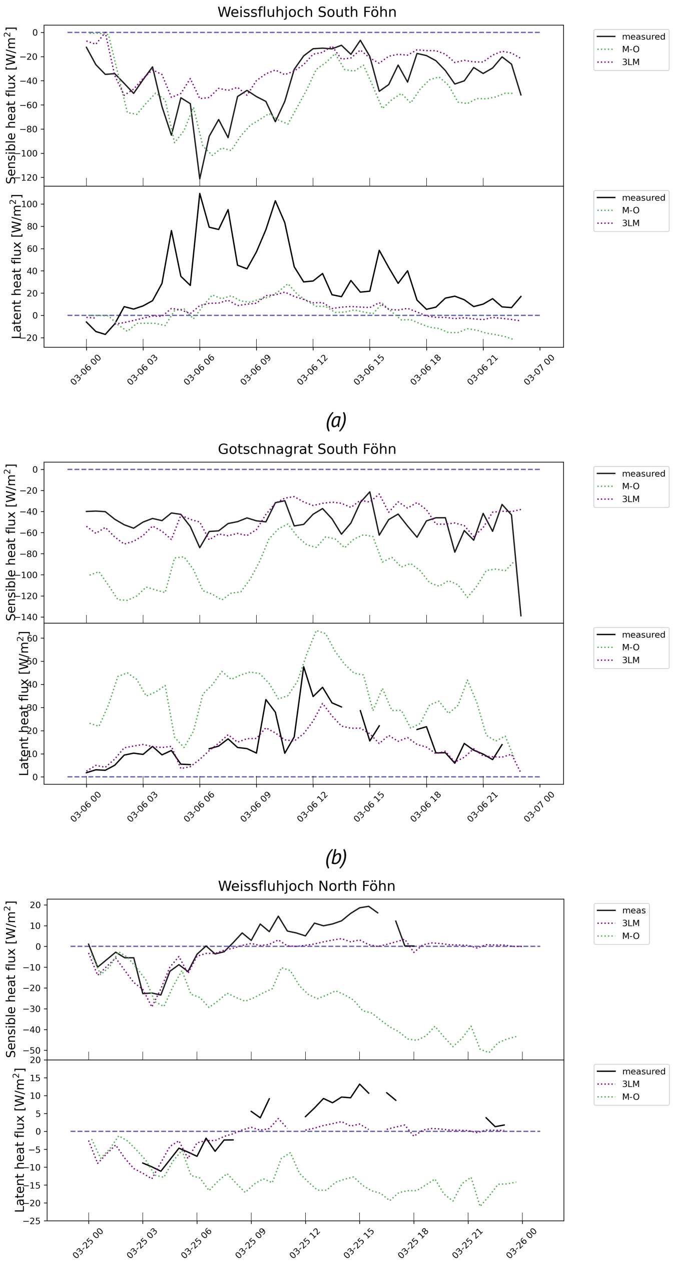

(a)

(b)

(c)

Figure 19: A comparison of turbulent fluxes latent and sensible at computed with eddy covariance (EC) in black, the 3-Layer Model (3LM) in pink, and Monin-Obukhov (M-O) in green. Figure a) shows the results for the south föhn event at WFJ, figure b) for the south föhn event at GOT, and figure c) for the north föhn at WFJ. There are significant discrepancies between M-O and the other two methods for the north föhn event, the 3LM performs better than M-O.

6 Conclusions

This thesis investigates the spatial and temporal variability of turbulent fluxes in complex terrain over snow during different weather events. To accomplish this, we employ two distinct approaches. First, we use measurements of turbulent fluxes of latent and sensible heat obtained from two stations in mountain terrain in Switzerland to capture the local temporal variability for a single point. Subsequently, to assess if these point measurements are representative across the whole terrain, we use the state-of-the-art model CRYOWRF to model the spatial variability of these turbulent fluxes.

Comparing point measurements of turbulent fluxes measured with eddy covariance to those represented in the model revealed several discrepancies. A model resolution of 200 m fails to capture the local variability of wind velocity observed in the measurements accurately, resulting in differences in the turbulent fluxes. Additionally, some assumptions lying within the parameterizations of the model induce differences. Discrepancies between turbulent fluxes measured via eddy covariance and those computed using the Monin-Obukhov Similarity theory highlight the limitations of employing M-O parametrizations in complex terrain. Since the model relies on this M-O method for turbulent flux computation and maintains a constant roughness length across all snow-covered surfaces, differences arise between eddy covariance measured fluxes and the model predictions. To further improve models for representing local turbulent fluxes, a higher resolution is necessary to accurately represent local variations in the wind field. Additionally, adaptations to the M-O theory for complex terrain and the incorporation of variable roughness length based on terrain complexity are essential.

Despite these disparities, the results of the model still provide insights into the larger-scale variability of the energy exchange by turbulent fluxes. One key finding is the substantial spatial variability of turbulent fluxes, indicating that point measurements do not represent the entire terrain. The magnitude and direction of turbulent fluxes can vary significantly within the mountain ridge scale. The wind field is the main driver of this spatial variability. However, the extent of this influence by wind is dependent on the synoptic weather pattern. During föhn events, differences between air and surface temperatures throughout elevations lead to an elevation dependence of the turbulent fluxes, which creates a correlation between wind and turbulent flux per elevation.

The synoptic weather pattern present substantially influences the magnitude of the turbulent fluxes, leading to a possible large contribution to the total energy balance of the snowpack. During the modeled south föhn day, certain areas within the domain receive a greater energy input from sensible heat flux than from net shortwave radiation. This highlights the importance of accurately representing turbulent fluxes in snowpack modeling. The spatial variability observed in turbulent fluxes holds significance for hydrological modeling and avalanche forecasting purposes. This variability can lead to significant differences in melt rates or energy input to the snowpack.

Additionally, the resolution of the model leads to significant differences in the modeled turbulent fluxes. Primarily, coarser (1 km) resolutions overestimate wind velocities compared to higher (200 m) resolutions. Consequentially, domain-wide daily average fluxes are twice the magnitude in coarser resolution compared to higher resolution simulations. In contrast to other studies, the contribution of blowing snow sublimation to total sublimation is minimal and localized over short time scales in our domain.

References

Andreas, E. L. (2002). Parameterizing scalar transfer over snow and ice: A review. *Journal of Hydrometeorology*, *3*(4), 417–432.

Burba, G. G., McDERMITT, D. K., Grelle, A., Anderson, D. J., & Xu, L. (2008). Addressing the influence of instrument surface heat exchange on the measurements of co2 flux from open-path gas analyzers. *Global Change Biology*, *14*(8), 1854–1876.

Businger, J. (1986). Evaluation of the accuracy with which dry deposition can be measured with current micrometeorological techniques. *Journal of Applied Meteorology and Climatology*, *25*(8), 1100–1124.

Clifton, A., Rüedi, J.-D., & Lehning, M. (2006). Snow saltation threshold measurements in a drifting-snow wind tunnel. *Journal of Glaciology*, *52*(179), 585–596.

DeBeer, C. M., & Pomeroy, J. W. (2017). Influence of snowpack and melt energy heterogeneity on snow cover depletion and snowmelt runoff simulation in a cold mountain environment. *Journal of hydrology*, *553*, 199–213.

Denby, B. (1999). Second-order modelling of turbulence in katabatic flows. *Boundary-Layer Meteorology*, *92*, 65–98.

Doyle, J. D., Volkert, H., Dörnbrack, A., Hoinka, K. P., & Hogan, T. F. (2002). Aircraft measurements and numerical simulations of mountain waves over the central alps: A pre-map test case. *Quarterly Journal of the Royal Meteorological Society: A journal of the atmospheric sciences, applied meteorology and physical oceanography*, *128*(584), 2175–2184.

Dudhia, J. (2010). Wrf physics options. *NCAR WRF basic tutorial*, *26*, 30.

Egli, L., Jonas, T., Grünewald, T., Schirmer, M., & Burlando, P. (2012). Dynamics of snow ablation in a small alpine catchment observed by repeated terrestrial laser scans. *Hydrological Processes*, *26*(10), 1574–1585.

Elvidge, A. D., & Renfrew, I. A. (2016). The causes of foehn warming in the lee of mountains. *Bulletin of the American Meteorological Society*, *97*(3), 455–466.

Foken, T., & Wichura, B. (1996). Tools for quality assessment of surface-based flux measurements. *Agricultural and forest meteorology*, *78*(1-2), 83–105.

Foken, T. (2006). 50 years of the monin–obukhov similarity theory. *Boundary-Layer Meteorology*, *119*, 431–447.

Foken, T., Göockede, M., Mauder, M., Mahrt, L., Amiro, B., & Munger, W. (2004). Post-field data quality control. In *Handbook of micrometeorology: A guide for surface flux measurement and analysis* (pp. 181–208). Springer.

Foken, T., & Nappo, C. J. (2008). *Micrometeorology* (Vol. 2). Springer.

Gauer, P. (1999). *Blowing and drifting snow in alpine terrain: A physically-based numerical model and related field measurements* [Doctoral dissertation, ETH Zurich].

Gohm, A., Zängl, G., & Mayr, G. J. (2004). South foehn in the wipp valley on 24 october 1999 (map iop 10): Verification of high-resolution numerical simulations with observations. *Monthly weather review*, *132*(1), 78–102.

González-Herrero, S., Sigmund, A., Haugeneder, M., Hames, O., Huwald, H., Fiddes, J., & Lehning, M. (2024). Using the sensible heat flux eddy covariance-based exchange coefficient to calculate latent heat flux from moisture mean gradients over snow. *Boundary-Layer Meteorology*, *190*(5), 1–22.

Groot Zwaaftink, C. D., Mott, R., & Lehning, M. (2013). Seasonal simulation of drifting snow sublimation in alpine terrain. *Water Resources Research*, *49*(3), 1581–1590.

Haugeneder, M., Lehning, M., Reynolds, D., Jonas, T., & Mott, R. (2023). A novel method to quantify near-surface boundary-layer dynamics at ultra-high spatio-temporal resolution. *Boundary-Layer Meteorology*, *186*(2), 177–197.

Helbig, N., van Herwijnen, A., Magnusson, J., & Jonas, T. (2015). Fractional snow-covered area parameterization over complex topography. *Hydrology and Earth System Sciences*, *19*(3), 1339–1351.

Holtslag, A., & De Bruin, H. (1988). Applied modeling of the nighttime surface energy balance over land. *Journal of Applied Meteorology and Climatology*, *27*(6), 689–704.

Howell, J., & Mahrt, L. (1997). Multiresolution flux decomposition. *Boundary-Layer Meteorology*, *83*, 117–137.

Judith, J., & Doorschot, J. (2004). Field measurements of snow-drift threshold and mass fluxes, and related mold simulations. *Bound-Lay Meteorol*, *113*, 347–368.

Kristianti, F., Gerber, F., González-Herrero, S., Dujardin, J., Huwald, H., Hoch, S. W., & Lehning, M. (2024). Influence of air flow features on alpine wind energy potential. *Frontiers in Energy Research*, *12*, 1379863.

Lehner, M., & Rotach, M. W. (2018). Current challenges in understanding and predicting transport and exchange in the atmosphere over mountainous terrain. *Atmosphere*, *9*(7), 276.

Lehning, M., Löwe, H., Ryser, M., & Raderschall, N. (2008). Inhomogeneous precipitation distribution and snow transport in steep terrain. *Water Resources Research*, *44*(7).

Lehning, M., Bartelt, P., Brown, B., & Fierz, C. (2002). A physical snowpack model for the swiss avalanche warning: Part iii: Meteorological forcing, thin layer formation and evaluation. *Cold Regions Science and Technology*, *35*(3), 169–184.

Lehning, M., Bartelt, P., Brown, B., Russi, T., Stöckli, U., & Zimmerli, M. (1999). Snowpack model calculations for avalanche warning based upon a new network of weather and snow stations. *Cold Regions Science and Technology*, *30*(1-3), 145–157.

Mahrt, L. (1999). Stratified atmospheric boundary layers. *Boundary-Layer Meteorology*, *90*, 375–396.

Mahrt, L. (2014). Stably stratified atmospheric boundary layers. *Annual Review of Fluid Mechanics*, *46*, 23–45.

Massman, W. (2000). A simple method for estimating frequency response corrections for eddy covariance systems. *Agricultural and Forest Meteorology*, *104*(3), 185–198.

Mauder, M., Cuntz, M., Drüe, C., Graf, A., Rebmann, C., Schmid, H. P., Schmidt, M., & Steinbrecher, R. (2013). A strategy for quality and uncertainty assessment of long-term eddy-covariance measurements. *Agricultural and Forest Meteorology*, *169*, 122–135.

Moncrieff, J., Clement, R., Finnigan, J., & Meyers, T. (2004). Averaging, detrending, and filtering of eddy covariance time series. In *Handbook of micrometeorology: A guide for surface flux measurement and analysis* (pp. 7–31). Springer.

Mott, R., Egli, L., Grünewald, T., Dawes, N., Manes, C., Bavay, M., & Lehning, M. (2011). Micrometeorological processes driving snow ablation in an alpine catchment. *The Cryosphere*, *5*(4), 1083–1098.

Mott, R., Vionnet, V., & Grünewald, T. (2018). The seasonal snow cover dynamics: Review on wind-driven coupling processes. *Frontiers in Earth Science*, *6*, 197.

Naaim, M., Naaim-Bouvet, F., & Martinez, H. (1998). Numerical simulation of drifting snow: Erosion and deposition models. *Annals of glaciology*, *26*, 191–196.

National Geospatial-Intelligence Agency (NGA). (2000). Shuttle radar topography mission 1-arc second global. http://srtm.usgs.gov/mission.php

Panofsky, H. (1984). Vertical variation of roughness length at the boulder atmospheric observatory. *Boundary-layer meteorology*, *28*, 305–308.

Pohl, S., Marsh, P., & Liston, G. (2006). Spatial-temporal variability in turbulent fluxes during spring snowmelt. *Arctic, Antarctic, and Alpine Research*, *38*(1), 136–146.

Pomeroy, J., & Essery, R. (1999). Turbulent fluxes during blowing snow: Field tests of model sublimation predictions. *Hydrological Processes*, *13*(18), 2963–2975.

Rotach, M. W., & Zardi, D. (2007). On the boundary-layer structure over highly complex terrain: Key findings from map. *Quarterly Journal of the Royal Meteorological Society: A journal of the atmospheric sciences, applied meteorology and physical oceanography*, *133*(625), 937–948.

Schlögl, S., Lehning, M., Nishimura, K., Huwald, H., Cullen, N. J., & Mott, R. (2017). How do stability corrections perform in the stable boundary layer over snow? *Boundary-Layer Meteorology*, *165*, 161–180.

Serafin, S., Adler, B., Cuxart, J., De Wekker, S. F., Gohm, A., Grisogono, B., Kalthoff, N., Kirshbaum, D. J., Rotach, M. W., Schmidli, J., et al. (2018). Exchange processes in the atmospheric boundary layer over mountainous terrain. *Atmosphere*, *9*(3), 102.

Sharma, V., Gerber, F., & Lehning, M. (2021). Introducing cryowrf v1. 0: Multiscale atmospheric flow simulations with advanced snow cover modelling. *Geoscientific Model Development Discussions*, *2021*, 1–46.

Sigmund, A., Dujardin, J., Comola, F., Sharma, V., Huwald, H., Melo, D. B., Hirasawa, N., Nishimura, K., & Lehning, M. (2022). Evidence of strong flux underestimation by bulk parametrizations during drifting and blowing snow. *Boundary-Layer Meteorology*, *182*(1), 119–146.

Sodemann, H., & Foken, T. (2005). Special characteristics of the temperature structure near the surface. *Theoretical and applied climatology*, *80*, 81–89.

Stiperski, I., & Calaf, M. (2018). Dependence of near-surface similarity scaling on the anisotropy of atmospheric turbulence. *Quarterly Journal of the Royal Meteorological Society*, *144*(712), 641–657.

Stiperski, I., & Calaf, M. (2023). Generalizing monin-obukhov similarity theory (1954) for complex atmospheric turbulence. *Physical Review Letters*, *130*(12), 124001.

Stiperski, I., & Rotach, M. W. (2016). On the measurement of turbulence over complex mountainous terrain. *Boundary-Layer Meteorology*, *159*, 97–121.

Strasser, U., Bernhardt, M., Weber, M., Liston, G., & Mauser, W. (2008). Is snow sublimation important in the alpine water balance? *The Cryosphere*, *2*(1), 53–66.

Thomas, C., & Foken, T. (2002). P2. 3 re-evaluation of integral turbulence characteristics and their parameterisations. *Symposium on Boundary Layers and Turbulence*, *15*, 129.

Umek, L., Gohm, A., Haid, M., Ward, H., & Rotach, M. (2021). Large-eddy simulation of foehn–cold pool interactions in the inn valley during piano iop 2. *Quarterly Journal of the Royal Meteorological Society*, *147*(735), 944–982.

LI-COR. (2021). Eddy covariance processing software.

Vionnet, V., Martin, E., Masson, V., Guyomarc'h, G., Naaim-Bouvet, F., Prokop, A., Durand, Y., & Lac, C. (2014). Simulation of wind-induced snow transport and sublimation in alpine terrain using a fully coupled snowpack/atmosphere model. *The Cryosphere*, *8*(2), 395–415.

Webb, E. K., Pearman, G. I., & Leuning, R. (1980). Correction of flux measurements for density effects due to heat and water vapour transfer. *Quarterly Journal of the Royal Meteorological Society*, *106*(447), 85–100.

Wilczak, J. M., Oncley, S. P., & Stage, S. A. (2001). Sonic anemometer tilt correction algorithms. *Boundary-layer meteorology*, *99*, 127–150.

A Appendix A

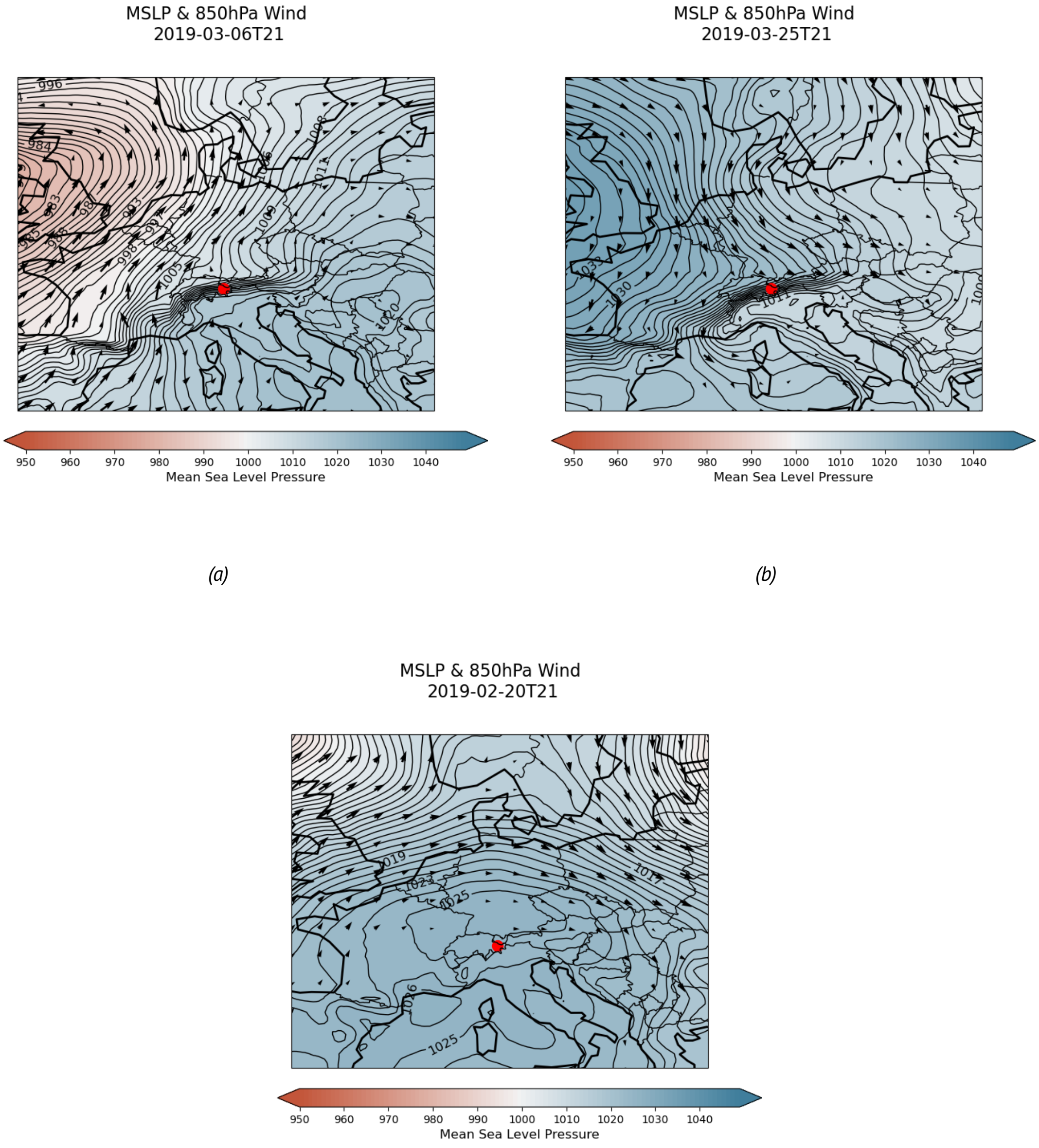

(a)

(b)

(c)

Figure A.1: Maps of the mean sea level pressure and synoptic large-scale flow over the European continent for the south föhn (a), north föhn (b), and calm day (c). The black line denotes the isobars and the arrows denote the wind direction and speed at 850 hPa. Red shows areas of low pressure and blue areas of high pressure.

B Appendix B

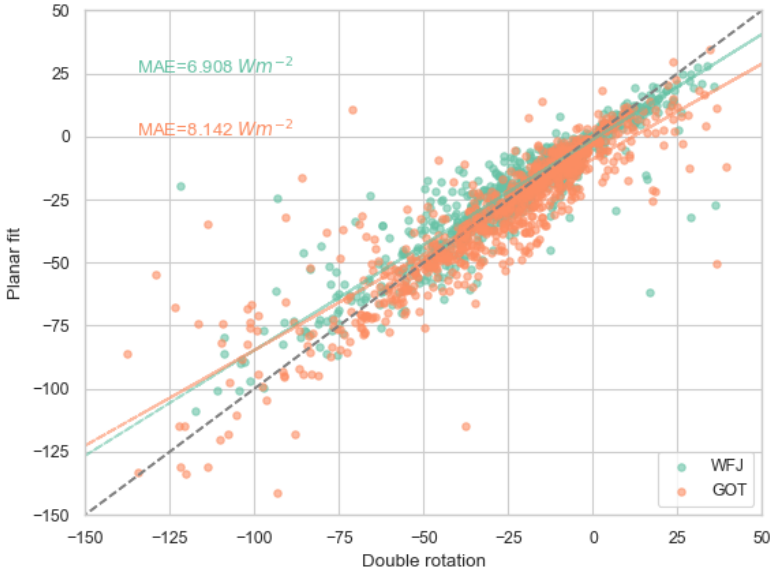

Figure B.1: Scatter plot of sensible heat flux processed with two different tilt correction methods, the Planar Fit and Double rotation method, for WFJ (green) and GOT (orange).

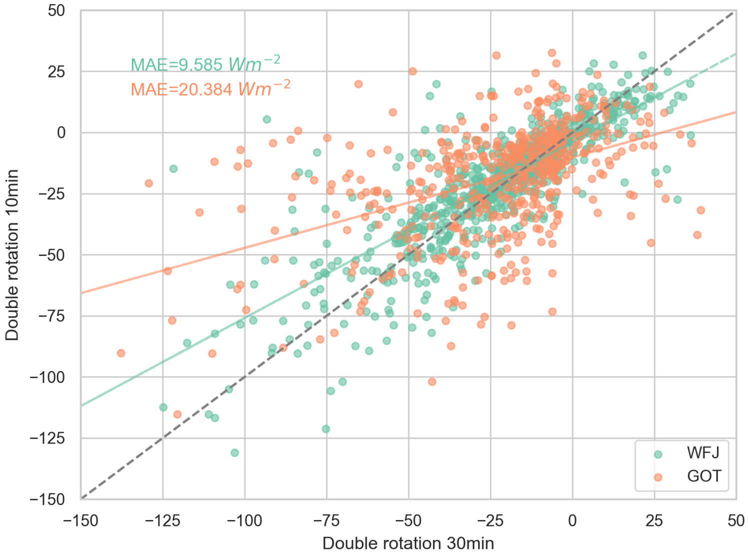

Figure B.2: Scatter plot of sensible heat flux processed with two different time-averaging intervals, of 30 minutes and 10 minutes, for WFJ (green) and GOT (orange).

C Appendix C

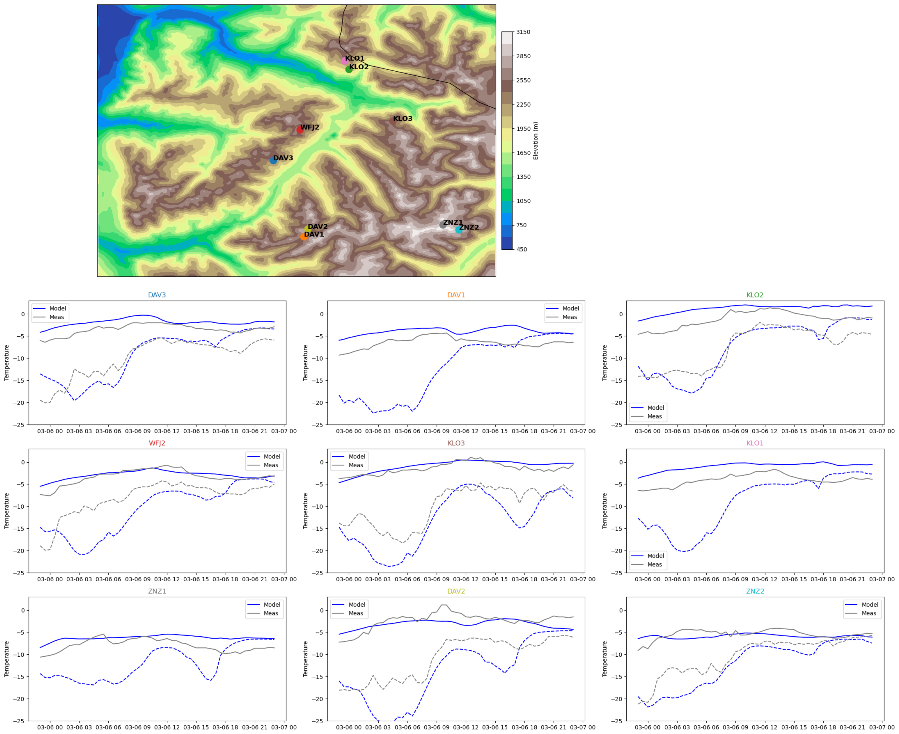

(a) Temperature

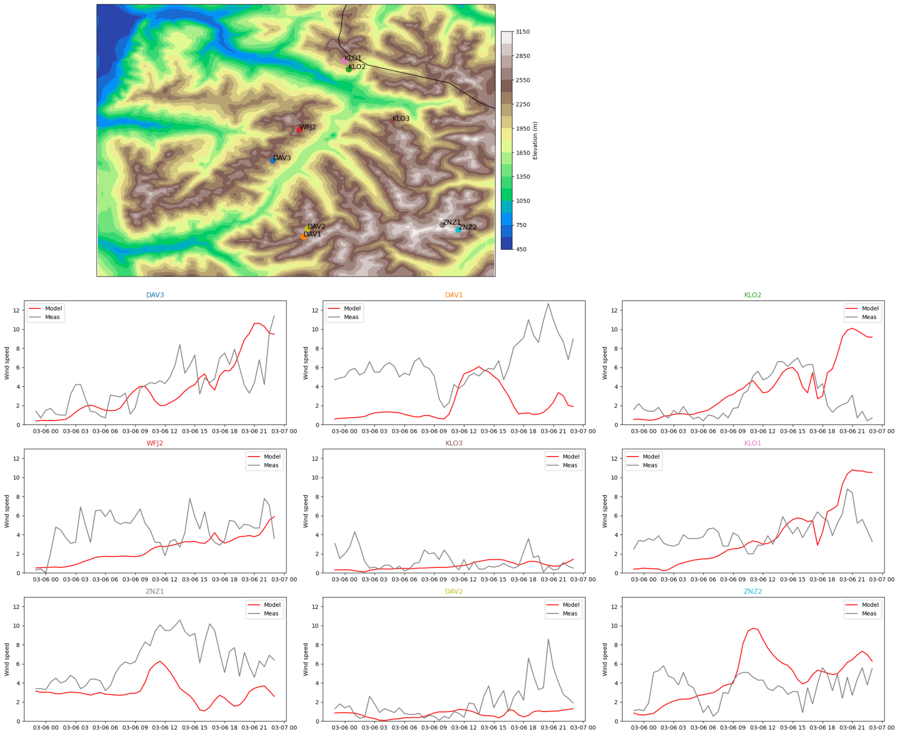

(b) Wind

Figure C.1: Model domain 5 (200 m) compared to measurements by IMIS stations of temperature (a) and wind speed (b) for the south föhn day. The locations of the stations are given on the map and are all situated in the mountains.

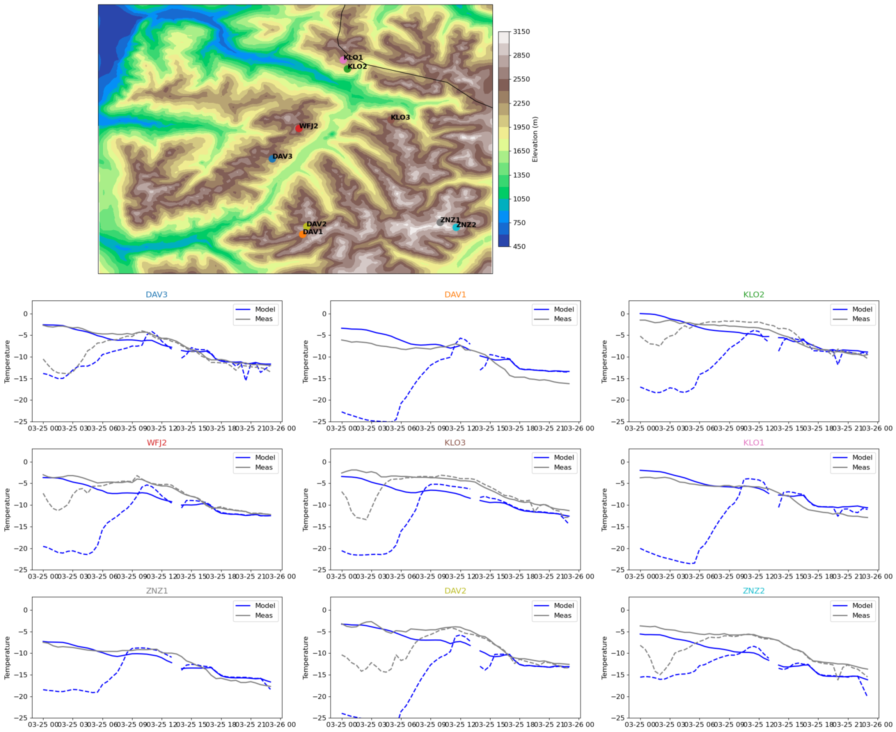

(a) Temperature

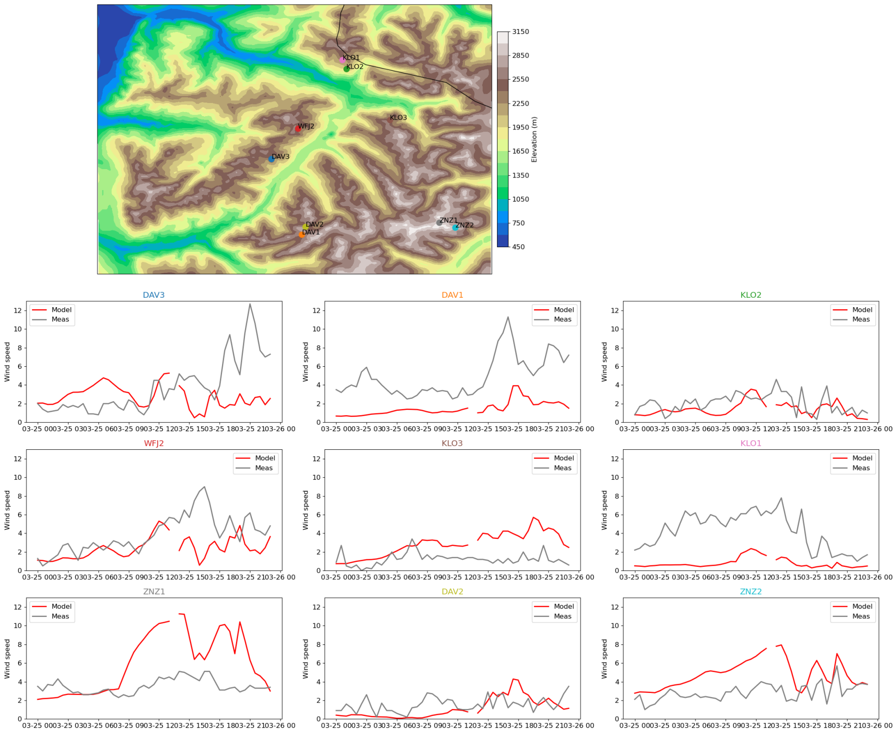

(b) Wind

Figure C.2: Model domain 5 (200 m) compared to measurements by IMIS stations of temperature (a) and wind speed (b) for the north föhn day. The locations of the stations are given on the map and are all situated in the mountains.

D Appendix D

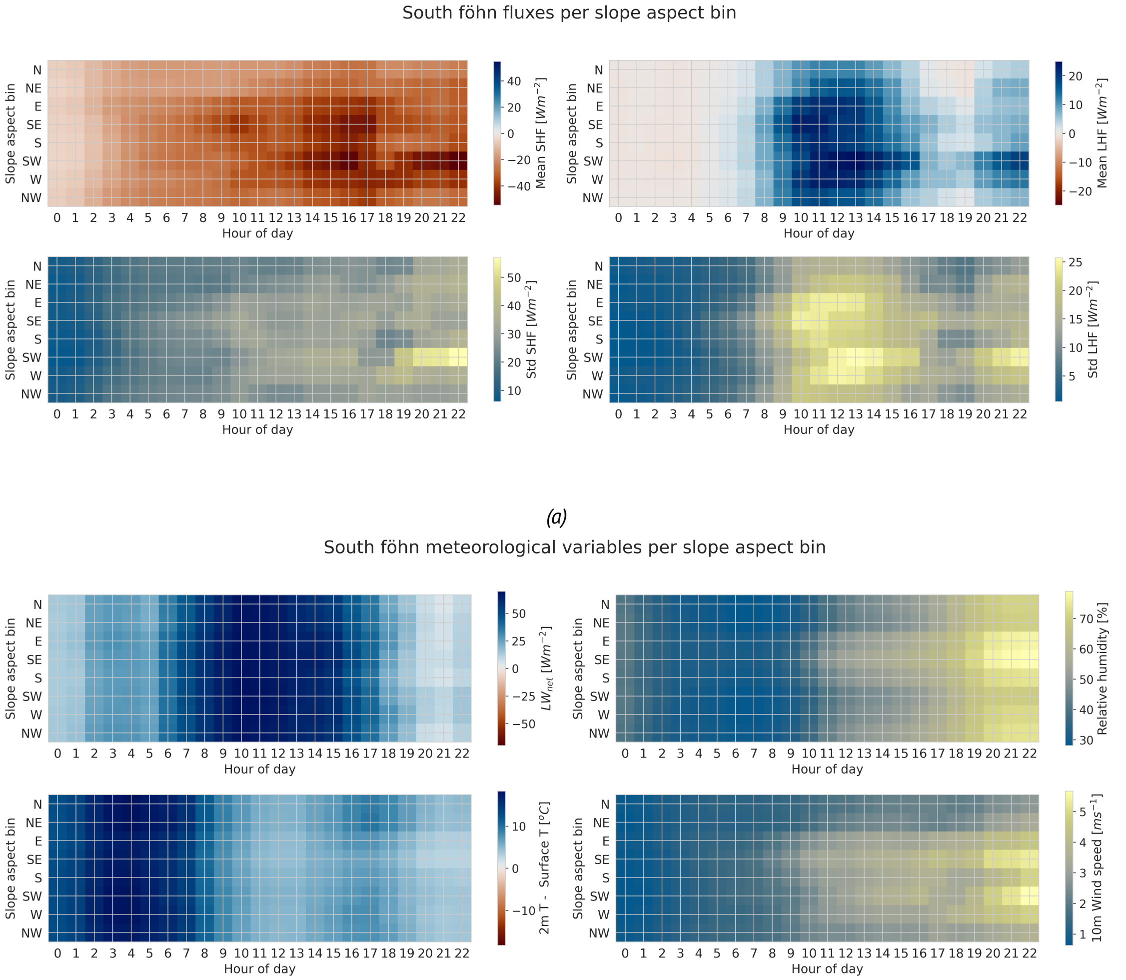
South föhn fluxes per slope aspect bin

(a)

South föhn meteorological variables per slope aspect bin

(b)

Figure D.1: The spatial and temporal evolution of sensible and latent heat flux with its standard deviation (a) and atmospheric variables of net longwave radiation, the difference between 2 m air and surface temperature, relative humidity, and 10 m wind velocity (b) throughout slope aspect for the south föhn. The aspect is the direction the slope is facing towards.

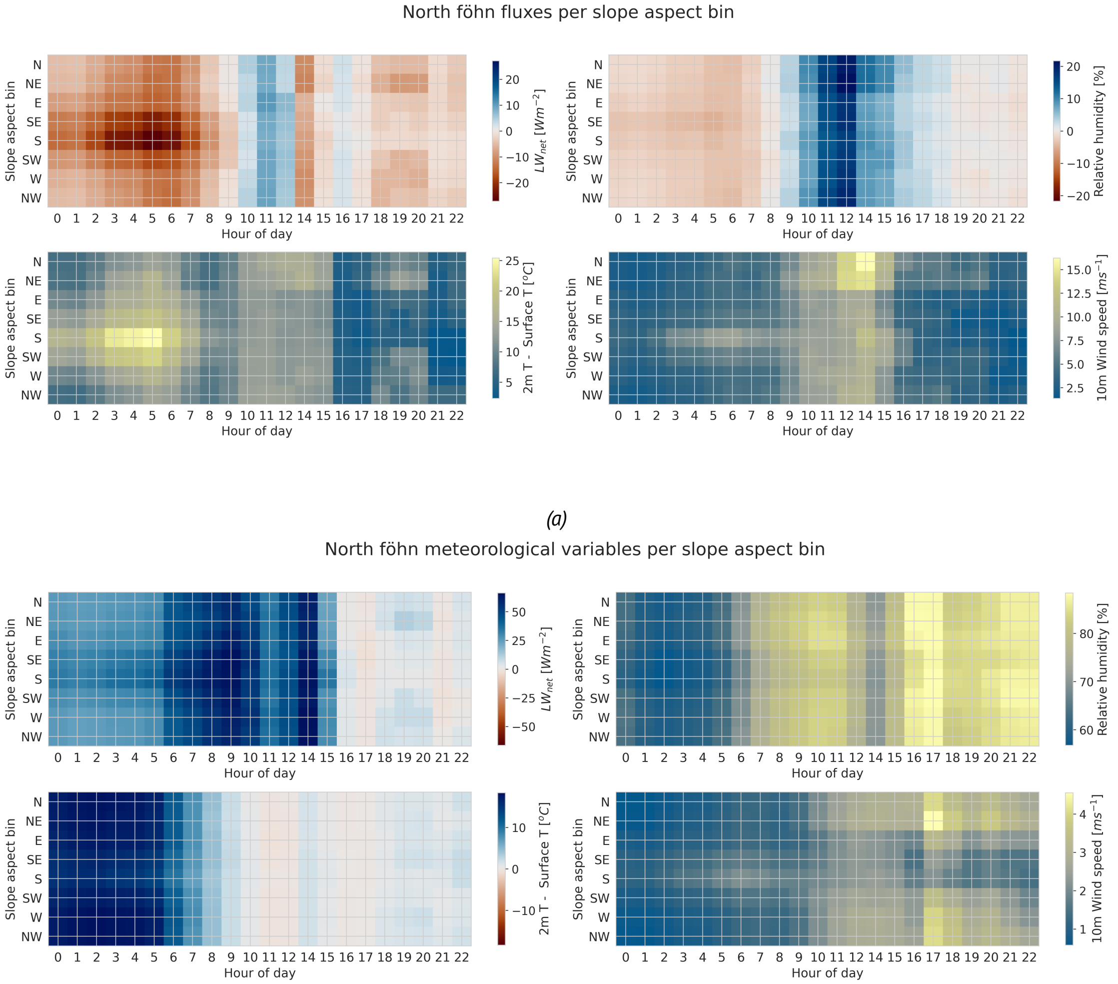

(a)

(b)

Figure D.2: The spatial and temporal evolution of sensible and latent heat flux with its standard deviation (a) and atmospheric variables of net longwave radiation, the difference between 2 m air and surface temperature, relative humidity, and 10 m wind velocity (b) throughout slope aspect for the south föhn. The aspect is the direction the slope is facing towards.

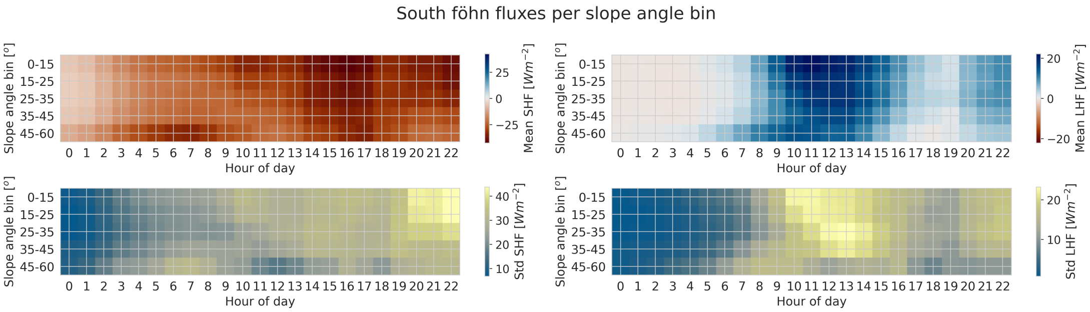

(a)

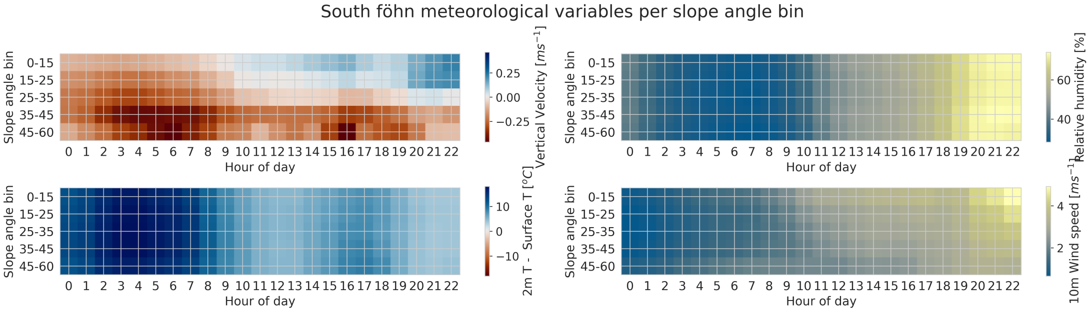

(b)

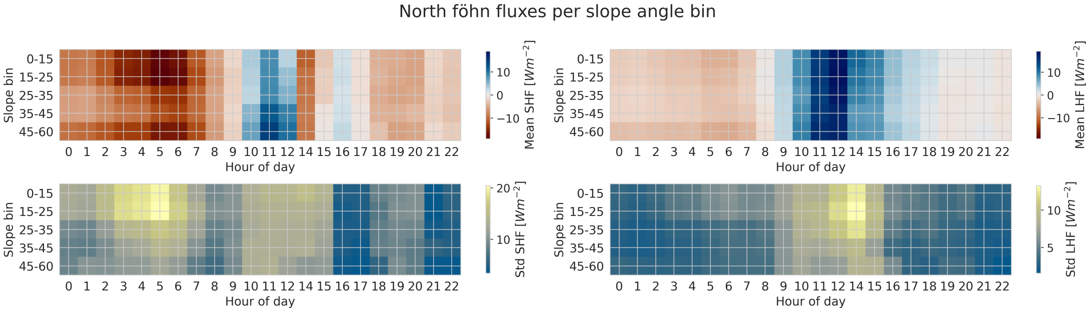

(c)

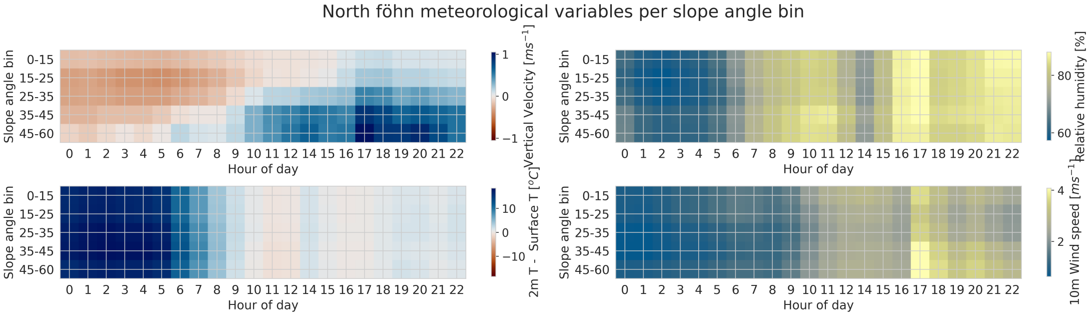

(d)

Figure D.3: The spatial and temporal evolution of sensible and latent heat flux with its standard deviation throughout slope angles for south föhn (a) and the north föhn (c). Meteorological variables of vertical wind velocity for the lowest vertical gridpoint, the difference between 2 m air and surface temperature, relative humidity, and 10 m wind speed are given in (b) and (d).